

# Imaging results from the legacy GMRT Galaxy Cluster Key Project

Lijo T. George<sup>1★</sup>, Ruta Kale<sup>1</sup>, and, Yogesh Wadadekar<sup>1</sup>

<sup>1</sup>*National Centre for Radio Astrophysics–Tata Institute of Fundamental Research, Ganeshkhind, Pune, Maharashtra, INDIA*

Accepted 2021 August 6. Received 2021 August 6; in original form 2021 May 18

## ABSTRACT

We have used archival GMRT data to image and study 39 galaxy clusters. These observations were made as part of the GMRT Key Project on galaxy clusters between 2001 and 2004. The observations presented in this sample include 14 observations at 610 MHz, 29 at 325 MHz and 3 at 244 MHz covering a redshift range of 0.02 to 0.62. Multi-frequency observations were made for 8 clusters. We analysed the clusters using the SPAM processing software and detected the presence of radio halo emission for the first time in the clusters RXC J0510-0801 and RXC J2211.7-0349. We also confirmed the presence of extended emission in 11 clusters which were known from the literature. In clusters where halos were not detected upper limits were placed using our own semi-automated program. We plot our detections and non-detections on the empirical  $L_X - P_{1.4}$  and  $M_{500} - P_{1.4}$  relation in radio halo clusters and discuss the results. The best fits follow a power law of the form  $L_{500} \propto P_{1.4}^{1.82}$  and  $M_{500} \propto P_{1.4}^{3.001}$  which is in accordance with the best estimates in the literature.

**Key words:**

## 1 INTRODUCTION

Galaxy clusters are the largest gravitationally bound objects in the Universe. Diffuse (surface brightness  $\sim \text{mJy arcmin}^{-2}$  at 1.4 GHz), extended ( $\sim \text{Mpc}$ ) radio emission from galaxy clusters is seen in the form of *radio halos* and *radio relics* (see Feretti et al. 2012; Brunetti & Jones 2014; van Weeren et al. 2019, for reviews). This is emission from the gas in the Intra Cluster Medium (ICM) and not associated with any galaxies. Radio halos are usually located near the centre of the cluster coincident with the X-ray distribution of the cluster while radio relics are usually located near the edge of the X-ray distribution towards the periphery of the cluster. Halos are generally smooth and circular in morphology whereas relics are usually elongated and arc-shaped.

Statistically, radio halos and relics are not very common in the Universe. Only around a third of the brightest, most massive galaxy clusters ( $L_X > 5 \times 10^{45} \text{ erg s}^{-1}$ ) have been found to host halos and relics (Giovannini et al. 1999; Venturi et al. 2007, 2008; Kale et al. 2013, 2015). Furthermore, the galaxy clusters also need to be highly disturbed (i.e. show signs of recent merger activity) for increased likelihood to detect the presence of a halo (Buote 2001; Cassano et al. 2010).

The physical origins of both radio halos and relics are still not completely understood. While it was earlier suggested

that relics trace the outgoing shocks produced during a cluster merger and thus accelerate the ICM electrons to relativistic energies via Diffusive Shock Acceleration (Blandford & Eichler 1987; Jones & Ellison 1991; Ensslin et al. 1998), recent studies suggest that such a mechanism would not be sufficiently efficient in accelerating electrons to the energies required (Vazza & Brüggen 2014; Vazza et al. 2015, 2016). The models to explain radio halo emission fall under two categories - turbulent acceleration (primary) or hadronic (secondary). The primary model suggests that the electrons in the ICM are accelerated to relativistic levels due to the turbulence generated in a cluster merger (Brunetti et al. 2001; Petrosian 2001). The fact that the majority of radio halos have been discovered in merging galaxy clusters seems to support this model. On the other hand, the secondary model predicts that relativistic electrons in galaxy clusters are a byproduct of the inelastic collisions between thermal and relativistic protons (Dennison 1980; Blasi & Colafrancesco 1999; Pfrommer & Enßlin 2004). The biggest shortcoming of this model is that it also predicts gamma rays to be produced via the same process but so far no such emission has been detected (Aharonian et al. 2009a,b; Ackermann et al. 2010; Aleksić et al. 2010). It is also suggested that electrons produced via the secondary model could be as much as 10 times weaker than those produced via the primary model (Brunetti & Lazarian 2011). It should be noted that the secondary model is not restricted by the dynamical state of the cluster.

★ E-mail: lijo7george@gmail.com

It has also been observed that radio halos exhibit an empirical correlation between their radio power at 1.4 GHz ( $P_{1.4}$ ) and the X-ray luminosity ( $L_X$ ) of their host galaxy cluster (Feretti 2000; Liang et al. 2000; Govoni et al. 2001; Bacchi et al. 2003; Brunetti et al. 2007, 2009). Since most halos have been detected in luminous galaxy clusters, this relation tends to hold true in that regime. However, if the secondary model is to be believed then there must also exist radio halos with weak radio power that the current generation of radio telescopes are not sensitive enough to detect. The next generation of radio interferometric telescopes like the Murchison Widefield Array (MWA) (Lonsdale et al. 2009; Bowman et al. 2013; Tingay et al. 2013), Australian SKA Pathfinder (ASKAP) (Johnston et al. 2009), LOw Frequency ARray (LOFAR) (van Haarlem et al. 2013) and the upcoming Square Kilometer Array (SKA) (Dewdney et al. 2013) are expected to improve in low surface brightness sensitivity and uv-coverage as compared to the existing telescopes. It is possible then that many new low radio power radio halos could be detected which will shed new light on the science behind their formation.

The Giant Metrewave Radio Telescope (GMRT) has been at the forefront of the study of radio halos and relics at low frequencies ( $< 1\text{GHz}$ ). The GMRT Radio Halo Survey (GRHS) (Venturi et al. 2007, 2008) and its follow up the extended GMRT Radio Halo Survey (eGRHS) (Kale et al. 2013, 2015) detected several radio halos, relics as well as mini-halos in a flux limited cluster sample. They also placed upper limits to halo emission in clusters where no halo was detected. These upper limits suggest a *bi-modal* nature of galaxy clusters in the  $L_X - P_{1.4}$  plot. While it is possible that these clusters truly do not contain any halos it is also possible that their detection is simply limited by the sensitivity limit of the GMRT. However, even before the (e)GRHS there was another attempt to observe and study extended emission from galaxy clusters with the GMRT.

### 1.1 GMRT Cluster Key Project

The GMRT Key Project was initiated by V. K. Kulkarni and Gopal-Krishna in 2001 with the aim of imaging a well-defined sample of galaxy clusters to search for sources of diffuse radio emission in them. Over the course of 5 GMRT cycles, 39 clusters were observed with the GMRT at 244, 325 and 610 MHz. There were 14 clusters observed at 610 MHz and only 3 observed at 244 MHz. The majority of the clusters (29) were observed at 325 MHz. Multi-frequency observations (2 or more frequency bands) were available for only 8 clusters. The aim when creating the sample was to map the parameter space across three axes: halo/relic radio luminosity, X-ray luminosity, and a quantifier of the cluster's dynamical state (inferred from the X-ray distribution). Furthermore, the project was to be complemented with X-ray observations from the *Chandra* and *XMM-Newton* telescopes which could be used to estimate the X-ray luminosity/temperature of the cluster and also quantify the dynamical state of the cluster.

The clusters in the sample ranged in redshift from 0.02 to 0.62. The motivation to observe clusters at moderate redshifts ( $z > 0.3$ ) was to look for evolutionary trends in the radio properties since merger activity is expected to be higher at intermediate redshifts.

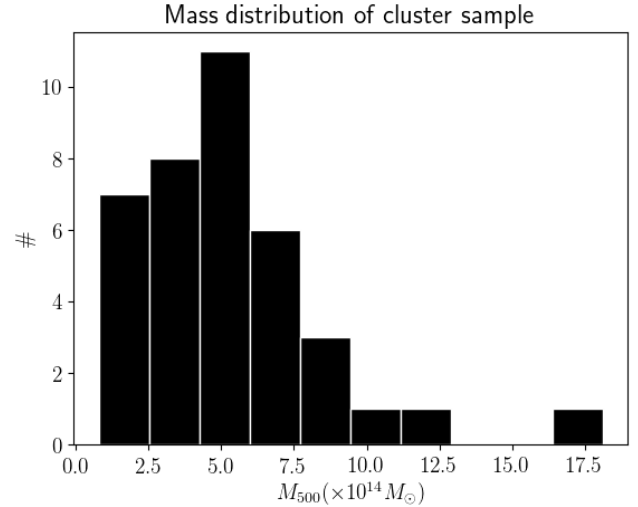


**Figure 1.** Histogram of the cluster mass ( $M_{500}$ ) of all the clusters in our sample.

Figure 1 shows the mass distribution of all the clusters in our sample. The masses have been obtained from the Meta-Catalogue of X-ray Clusters (MCXC, Piffaretti et al. (2011)). All the masses were obtained from various surveys based on the ROSAT All-Sky Survey (RASS, Truemper (1993)). The luminosities and masses of the clusters in the various surveys were homogenised to  $L_{500}$  and  $M_{500}$  by the authors. In our sample, the  $L_{500}$  ranges from  $0.22 \times 10^{44}$  erg  $\text{s}^{-1}$  to  $24 \times 10^{44}$  erg  $\text{s}^{-1}$ . We that no values could be found for the cluster RX J1046.8-2535. Note that  $L_{500}$  and  $M_{500}$  are the X-ray luminosity and mass of the cluster within the radius  $R_{500}$  of the cluster, where  $R_{500}$  is the radius at which the cluster mass density is 500 times the critical mass density of the Universe. The masses in particular were calculated from the X-ray luminosities using the luminosity mass relation for galaxy clusters as provided by Arnaud et al. (2010).

In Figure 2 we also compare all the clusters in our sample with all other clusters in the MCXC in an X-ray luminosity vs redshift plot.

In Section 2 we give the details about the observations and the software used for our analysis. In Section 3 we briefly discuss the results of our analysis including two new detections of radio halos. Finally, we end with Sections 4 and 5 with a discussion on our results including how non-detections were handled and the main conclusions of this paper. The cosmology used in this paper is as follows:  $\Omega_0 = 0.3, \Omega_{\Lambda} = 0.7, H_0 = 68$  km  $\text{s}^{-1}$  Mpc $^{-1}$ .

## 2 OBSERVATIONS AND ANALYSIS

The 39 clusters in this sample were observed between 11 January 2002 and 25 April 2004 which corresponds to Cycle 1 to Cycle 5 of the GMRT. Table 1 shows the list of clusters and the date they were observed along with the time spent on source at each frequency. These observations used the old GMRT hardware correlator as the backend.

We used the software SPAM (Intema 2014; Intema et al. 2017) to analyse the data initially. Subsequent analysis that required continuum uv-subtraction to image the extended

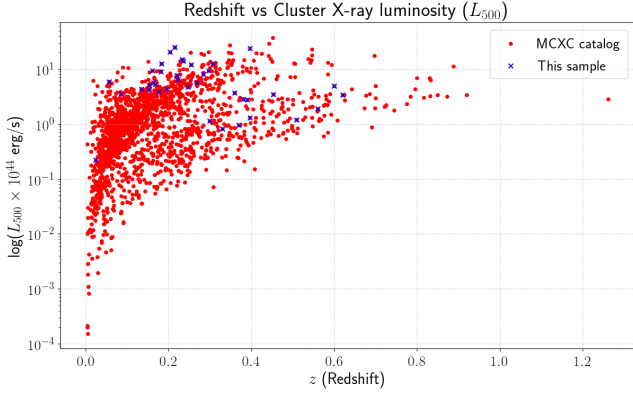


**Figure 2.** X-ray luminosity ( $L_{500}$ ) vs redshift plot of all the clusters in the MCXC (red) along with all the clusters in our sample (blue).

emission in the galaxy cluster were performed using the CASA software package (McMullin et al. 2007).

## 2.1 SPAM

SPAM (Source Peeling and Atmospheric Modeling) is a radio astronomy data processing software developed by Huib Intema. The software uses Parseltongue (Kettenis & Sijior 2012) and Orbit (Cotton 2013) as wrappers around the well-known software AIPS (Astronomical Image Processing Software) (Wells 1985) to provide a python interface for radio data processing. Several python packages like numpy and scipy are used in scripts that call on Parseltongue and subsequently AIPS for analysis.

The software uses the flux calibrator as the primary source for calibration and uses it to perform both flux and phase calibration on the target source. RFI (Radio Frequency Interference) mitigation is performed using a combination of outlier removal along the time and channel axes as well as modelling and subtraction of low level RFI and excision of particularly high amplitude data in the uv-plane with greater weights. Both direction-independent as well as direction-dependent calibration are performed by the software.

The raw visibility file is provided to SPAM which performs an initial calibration (using the primary calibrator) and RFI excision from the visibilities to produce a calibrated visibility file for all sources. In the next step, the target visibility file is processed while also undergoing further flagging and calibration (including self-calibration) during the process. The imaging parameters are provided at this stage. For our analysis, since we are interested in extended emission we used the *briggs* weighting scheme with a *robust* value of 0. This provides a decent compromise between sensitivity and resolution that we require. The final image produced at the end of this process is used for analysis. All other SPAM configuration parameters were kept at their default values.

Since all of the data used in this work was recorded with the old GMRT correlator an additional step was sometimes required at the beginning of the process. In cases where the data was split into the upper side-band (USB) and lower side-band (LSB) the data had to be combined before processing it through SPAM. This is also done using the `combine_usb_lsb` task in SPAM.

**Table 1.** Cluster list with date of observation and time on source

| Source           | Frequency (MHz) | Date of Observation (dd-mm-yyyy) | Time on Source (min) |
|------------------|-----------------|----------------------------------|----------------------|
| RX J1334.3+5030  | 610             | 11/01/2002                       | 417                  |
|                  | 325             | 22/08/2002                       | 134                  |
| RX J0505.3-2849  | 610             | 07/09/2002                       | 254                  |
|                  | 610             | 11/01/2002                       | 202                  |
| RX J1241.5+3250  | 325             | 06/02/2003                       | 416                  |
|                  | 610             | 11/01/2002                       | 378                  |
| RXJ0256.5+0006   | 610             | 12/01/2002                       | 311                  |
| RX J0318.2-0301  | 325             | 21/08/2002                       | 316                  |
|                  | 610             | 02/05/2002                       | 152                  |
| RX J1200.8-0327  | 325             | 01/03/2002                       | 225                  |
|                  | 325             | 02/03/2002                       | 74                   |
|                  | 610             | 02/05/2002                       | 277                  |
|                  | 610             | 02/06/2002                       | 169                  |
| Abell 2597       | 610             | 03/05/2002                       | 336                  |
| RX J0426.1+1655  | 244             | 19/07/2002                       | 249                  |
|                  | 325             | 02/03/2002                       | 261                  |
|                  | 610             | 06/09/2002                       | 256                  |
|                  | 610             | 02/06/2002                       | 274                  |
| RX J2237.0-1516  | 325             | 02/03/2002                       | 261                  |
|                  | 610             | 11/01/2002                       | 297                  |
|                  | 610             | 02/06/2002                       | 169                  |
| Abell 2319       | 325             | 02/06/2002                       | 253                  |
| Abell 2163       | 325             | 29/12/2003                       | 380                  |
|                  | 610             | 17/07/2002                       | 206                  |
| Abell 2345       | 610(E)          | 06/09/2002                       | 41                   |
|                  | 610(E)          | 07/09/2002                       | 115                  |
|                  | 610(W)          | 06/09/2002                       | 41                   |
|                  | 610(W)          | 07/09/2002                       | 162                  |
| RX J1701.3+6414  | 325             | 21/08/2002                       | 189                  |
| Abell 2390       | 244             | 18/07/2002                       | 200                  |
| Abell 665        | 244             | 19/07/2002                       | 229                  |
| RXC J1308.5+5342 | 325             | 14/02/2003                       | 392                  |
|                  | 610             | 19/12/2002                       | 382                  |
| RX J0847.1+3449  | 325             | 05/02/2003                       | 318                  |
|                  | 610             | 19/12/2002                       | 333                  |
| Abell 0400       | 325             | 05/02/2003                       | 251                  |
| RX J1120.1+4318  | 325             | 13/02/2003                       | 361                  |
| Abell 1084       | 325             | 19/07/2003                       | 798                  |
| RXC J2211.7-0349 | 325             | 19/07/2003                       | 761                  |
| Abell 0545       | 325             | 19/07/2003                       | 521                  |
| Abell 1689       | 325             | 20/07/2003                       | 413                  |
| RXC J2014.8-2430 | 325             | 20/07/2003                       | 497                  |
| Abell 0901       | 325             | 29/12/2003                       | 372                  |
| Abell 0291       | 325             | 29/12/2003                       | 468                  |
| RXC J1212.3-1816 | 325             | 31/12/2003                       | 612                  |
| RXJ1046.8-2535   | 325             | 19/01/2004                       | 427                  |
| Abell 2104       | 325             | 19/01/2004                       | 418                  |
| RXC J0510.7-0801 | 325             | 19/01/2004                       | 499                  |
| AS0780           | 325             | 20/01/2004                       | 504                  |
| Abell 2485       | 325             | 19/01/2004                       | 513                  |
| RXC J0437.1+0043 | 325             | 25/04/2004                       | 402                  |
| Abell 0907       | 325             | 25/04/2004                       | 63                   |
| Abell 3444       | 325             | 25/04/2004                       | 126                  |
| Abell 1300       | 325             | 25/04/2004                       | 252                  |
| RXC J1504.1-0248 | 325             | 25/04/2004                       | 282                  |
| RXC J1514.9-1523 | 325             | 25/04/2004                       | 292                  |
| Abell 2537       | 325             | 25/04/2004                       | 493                  |

### **3 RESULTS**

Table 2 contains the list of all clusters as well as some information about the clusters and the images produced with SPAM.

**Table 2.** Cluster list. Col. 1: Source Name, Col. 2: Redshift, Col. 3: Right Ascension (J2000), Col. 4: Declination (J2000), Col. 5: X-ray Luminosity in the [0.1-2.4] keV range<sup>1</sup>, Col. 6: Total mass<sup>1</sup>, Col. 7: Cluster radius<sup>1</sup>, Col. 8: Frequency of observation (MHz), Col. 9: RMS of the image, Col. 10: Beam size (in arcsec  $\times$  arcsec) and position angle (in degree).  
<sup>1</sup>These values and their definitions can be found in the MCXC (Piffaretti et al. 2011)

| Source           | $z$    | RA<br>hh:mm:ss | DEC<br>dd:mm:ss | $L_{500}$<br>$10^{44}$ erg s <sup>-1</sup> | $M_{500}$<br>$10^{14} \times M_{\odot}$ | $R_{500}$<br>Mpc | Frequency<br>MHz  | RMS<br>mJy beam <sup>-1</sup> | Beam size<br>(arcsec) $\times$ (arcsec), °   |
|------------------|--------|----------------|-----------------|--|---|------------------|-------------------|-------------------------------|--|
| RX J1334.3+5030  | 0.62   | 13:34:20.4     | 50:31:05.02     | 3.4056                                     | 2.6559                                  | 0.7786           | 610               | 0.15                          | 9.70 $\times$ 8.10, -74.99   |
| RX J0505.3-2849  | 0.509  | 05:05:19.9     | -28:49:05.2     | 1.1966                                     | 1.5420                                  | 0.6788           | 325<br>610        | 0.23<br>0.39                  | 13.44 $\times$ 8.68, -9.69<br>9.35 $\times$ 6.68, 12.86                                |
| RX J1241.5+3250  | 0.39   | 12:41:33.2     | 32:50:23        | 2.7505                                     | 2.8284                                  | 0.8704           | 325<br>610        | 0.16<br>0.10                  | 11.16 $\times$ 9.52, -16.92<br>5.50 $\times$ 5.10, -59.97                              |
| RX J0256.5+0006  | 0.36   | 02:56:33       | 00:06:12        | 3.6630                                     | 3.4520                                  | 0.941            | 610               | 0.18                          | 12.20 $\times$ 6.00, 88.84   |
| RX J0318.2-0301  | 0.37   | 03:18:17.5     | -03:01:14.02    | 0.9629                                     | 1.5161                                  | 0.7125           | 325<br>610        | 0.29<br>0.16                  | 11.40 $\times$ 8.30, 35.22<br>6.90 $\times$ 4.30, 59.23                                |
| RX J1200.8-0327  | 0.396  | 12:00:49.4     | -03:27:30       | 1.3039                                     | 1.7854                                  | 0.745            | 325<br>610        | 1.40<br>2.21                  | 26.22 $\times$ 11.40, 38<br>6.63 $\times$ 4.73, 3.8                                    |
| Abell 2597       | 0.0852 | 23:25:20       | -12:07:38       | 1.3039                                     | 1.7854                                  | 0.745            | 610               | 0.40                          | 9.00 $\times$ 6.26, -40.96   |
| RX J0426.1+1655  | 0.38   | 04:26:07.4     | 16:55:12        | 2.8406                                     | 2.9084                                  | 0.8820           | 244<br>325<br>610 | 1.18<br>0.53<br>1.48          | 22.12 $\times$ 10.79, 82.82<br>15.96 $\times$ 8.02, 57.88<br>5.61 $\times$ 4.05, 64.32 |
| RX J2237.0-1516  | 0.299  | 22:37:00.7     | -15:16:08       | 1.1314                                     | 1.7713                                  | 0.7709           | 325<br>610        | 0.25<br>0.08                  | 16.45 $\times$ 9.44, 60.86<br>6.70 $\times$ 4.30, 38.04                                |
| Abell 2319       | 0.0557 | 19:21:08.8     | 43:57:29.99     | 5.9418                                     | 5.8345                                  | 1.2483           | 610               | 0.06                          | 5.50 $\times$ 4.60, 29.31  |
| Abell 2163       | 0.203  | 16:15:34.13    | -06:07:26.29    | 20.1585                                    | 11.0518                                 | 1.4697           | 325<br>610        | 0.38<br>0.12                  | 13.76 $\times$ 9.55, 44.53<br>8.06 $\times$ 4.20, 55.69                                |
| Abell 2345       | 0.176  | 21:27:11       | -12:09:33.01    | 3.9026                                     | 4.1441                                  | 1.0699           | 610 (E)<br>610(W) | 0.38<br>0.43                  | 5.93 $\times$ 5.30, 36<br>7.13 $\times$ 4.62, 30                                       |
| RX J1701.3+6414  | 0.453  | 17:01:08.83    | 64:14:38.4      | 3.4926                                     | 3.1055                                  | 0.8763           | 325               | 0.24                          | 15.77 $\times$ 9.82, -5.18   |
| Abell 2390       | 0.2329 | 21:53:35.5     | 17:41:12.01     | 14.815                                     | 8.9525                                  | 1.3554           | 244               | 0.81                          | 18.50 $\times$ 13.68, 57.26  |
| Abell 665        | 0.1818 | 08:30:45.19    | 65:52:55.31     | 8.9977                                     | 6.8668                                  | 1.2635           | 244               | 0.74                          | 19.37 $\times$ 13.84, -6.7   |
| RXC J1308.5+5342 | 0.33   | 13:08:31.1     | 53:42:06.98     | 0.8107                                     | 1.4101                                  | 0.7062           | 325<br>610        | 0.12<br>0.05                  | 11.40 $\times$ 8.30, 35.22<br>6.3 $\times$ 4.7, 37.65                                  |
| RX J0847.1+3449  | 0.56   | 08:47:11.3     | 34:49:16        | 1.1916                                     | 1.9683                                  | 0.7216           | 325<br>610        | 0.10<br>0.06                  | 10.06 $\times$ 8.70, 26.6<br>6.9 $\times$ 4.7, 57.86                                   |
| Abell 0400       | 0.0238 | 02:56:30       | 06:10:00        | 0.2211                                     | 0.8012                                  | 0.6505           | 325               | 0.84                          | 10.01 $\times$ 9.50, 43.67   |
| RX J1120.1+4318  | 0.6    | 11:20:07.38    | 43:18:07.16     | 4.9580                                     | 3.3968                                  | 0.8519           | 325               | 0.17                          | 11.60 $\times$ 8.90, 28.99   |
| Abell 1084       | 0.1342 | 10:44:33       | -07:04:22       | 4.2956                                     | 4.5308                                  | 1.1182           | 325               | 0.20                          | 15.80 $\times$ 8.80, 62.54   |

**Table 2.** (continued) Cluster list

| Source           | $z$    | RA<br>hh:mm:ss | DEC<br>dd:mm:ss | $L_{500}$<br>$10^{44}$ erg s $^{-1}$ | $M_{500}$<br>$10^{14} \times M_{\odot}$ | $R_{500}$<br>Mpc | Frequency<br>MHz | RMS<br>mJy beam $^{-1}$ | Beam size<br>(arcsec) $\times$ (arcsec), $^{\circ}$ |
|------------------|--------|----------------|-----------------|--------------------------------------|---|------------------|------------------|-------------------------|---|
| RXC J2211.7-0349 | 0.397  | 22:11:44.6     | -03:49:47       | 24.0000                              | 18.1000                                 | 1.6100           | 325              | 0.20                    | 12.80 $\times$ 9.80, 72.06                          |
| Abell 0545       | 0.154  | 05:32:23.1     | -11:31:50.02    | 5.0062                               | 4.9028                                  | 1.1403           | 325              | 0.32                    | 12.70 $\times$ 8.80, 30.58                          |
| Abell 1689       | 0.1832 | 13:11:29.5     | -01:20:17.02    | 12.5240                              | 8.3920                                  | 1.3502           | 325              | 0.30                    | 12.20 $\times$ 8.40, 48.93                          |
| RXC J2014.8-2430 | 0.1612 | 20:14:50       | -24:30:35       | 9.4586                               | 7.1884                                  | 1.2922           | 325              | -                       | -   |
| Abell 0901       | 0.1634 | 09:56:26.4     | -10:04:12       | 5.6296                               | 5.2302                                  | 1.1613           | 325              | 0.2                     | 13.60 $\times$ 8.60, 39.77                          |
| Abell 0291       | 0.196  | 02:01:44.2     | -02:12:02.99    | 4.2718                               | 4.3137                                  | 1.0767           | 325              | 0.21                    | 11.30 $\times$ 10.40, -21.51                        |
| RXC J1212.3-1816 | 0.269  | 12:12:18.9     | -18:16:43       | 5.6441                               | 4.8327                                  | 1.0892           | 325              | 0.16                    | 15.10 $\times$ 9.60, 12.58                          |
| RXJ1046.8-2535   | 0.243  | 10:46:48       | -25:34:59.99    | -                                    | -                                       | -                | 325              | 0.16                    | 17.10 $\times$ 8.70, 34.55                          |
| Abell 2104       | 0.1533 | 15:40:07.5     | -03:18:29.02    | 4.2260                               | 4.4239                                  | 1.1021           | 325              | 0.45                    | 10.20 $\times$ 8.30, -80.66                         |
| RXC J0510.7-0801 | 0.2195 | 05:10:47.91    | -08:01:44.29    | 7.7286                               | 6.0827                                  | 1.1974           | 325              | 0.26                    | 14.60 $\times$ 8.50, 53.62                          |
| AS0780           | 0.2357 | 14:59:29.3     | -18:11:12.98    | 13.9675                              | 8.6180                                  | 1.3370           | 325              | 0.17                    | 14.30 $\times$ 9.60, -16.44                         |
| Abell 2485       | 0.2472 | 22:48:32.9     | -16:06:23       | 4.6638                               | 4.3759                                  | 1.0622           | 325              | 0.37                    | 12.86 $\times$ 9.43, 10.65                          |
| RXC J0437.1+0043 | 0.2842 | 04:37:10.1     | 00:43:37.99     | 8.0950                               | 5.9496                                  | 1.1608           | 325              | 0.21                    | 11.00 $\times$ 9.37, 50.02                          |
| Abell 0907       | 0.1669 | 09:58:22.2     | -11:03:34.99    | 5.2999                               | 5.0282                                  | 1.1448           | 325              | 0.59                    | 13.58 $\times$ 9.30, 55.59                          |
| Abell 3444       | 0.2542 | 10:23:50.8     | -27:15:31       | 11.9196                              | 7.7124                                  | 1.2798           | 325              | 0.46                    | 13.60 $\times$ 10.90, -10.11                        |
| Abell 1300       | 0.3075 | 11:31:54.4     | -19:55:41.99    | 12.4620                              | 7.5980                                  | 1.2485           | 325              | 0.72                    | 16.30 $\times$ 13.10, 30.19                         |
| RXC J1504.1-0248 | 0.2153 | 15:04:07.5     | -02:48:15.98    | 24.9688                              | 12.4750                                 | 1.5235           | 325              | 0.41                    | 14.30 $\times$ 9.30, 69.06                          |
| RXC J1514.9-1523 | 0.2226 | 15:14:58       | -15:23:10.0     | 6.4277                               | 5.4232                                  | 1.1511           | 325              | 0.26                    | 12.80 $\times$ 10.70, 59.53                         |
| Abell 2537       | 0.2966 | 23:08:23.2     | -02:11:30.98    | 9.3659                               | 6.4393                                  | 1.1864           | 325              | 0.25                    | 13.18 $\times$ 10.14, 82.04                         |



### 3.1 New Detections

In our sample of 38 clusters we have detected 2 new possible candidate radio halos - RXC J0510.7-0801 and RXC J2211.7-0349.

#### 3.1.1 RXC J0510.7-0801

This is a massive ( $M = 7.4 \times 10^{14} M_{\odot}$ ) (Giacintucci et al. 2017), luminous ( $L_X = 12.83 \times 10^{44} \text{ erg s}^{-1}$  Böhringer et al. (2004)) cluster at a redshift of  $z = 0.22$  (De Grandi et al. 1999). Kale et al. (2015) analysed this cluster but could not detect any extended emission as the quality of the data were poor.

Figure 3 shows the greyscale radio image of the cluster in the left panel. Also shown is the  $R_{500}$  range in the dashed circle. The right panel of the figure shows the contours of the radio image overlaid on the X-ray image from *XMM-Newton*. The bottom panel of the image shows the point source subtracted image smoothed and overlaid on the X-ray image. Point source subtraction was performed in CASA by first only imaging the point sources by setting the uv-cut-off above  $3k\lambda$  and then using the task UVSUB to remove the point sources from the visibility file. Finally, in order to bring out the extended emission better, imaging was performed using only the first  $5k\lambda$  using the modified visibility file.

#### 3.1.2 RXC J2211.7-0349

This is also an extremely massive ( $M_X = 10.5 \times 10^{14} M_{\odot}$ ) and luminous ( $L_X = 15.84 \times 10^{44} \text{ erg s}^{-1}$  (Ebeling et al. 2010)) cluster at a redshift of  $z = 0.3977$ . The gas temperature of the cluster was estimated to be  $T_X = 11.3^{+1.46}_{-1.17} \text{ keV}$  (Cavagnolo et al. 2008).

The radio image of this cluster is shown in the left panel of Fig. 4. The right panel shows the radio contours on the colour X-ray image. The X-ray image is also from the *XMM-Newton* as before. The bottom panel of the image shows the point source subtracted image smoothed and overlaid on the X-ray image. This image was also created using the same method as mentioned above for RXC J0510.7-0801.

Rossetti et al. (2016) studied this cluster as part of a *Planck* selected sample of clusters to characterize the dynamical state of clusters. For this cluster they used results from Wen et al. (2012) who cross-matched clusters between optical (SDSS) and X-ray (*ROSAT*) catalogs. Based on their analysis they estimated the X-ray peak of the cluster to be offset from the BCG in the cluster by  $7.16''$  (38.3 kpc).

In radio the cluster was observed with the GMRT again in 2009 (Project ID: 16\_117) at 610 MHz. We analysed these data as well using the same method described before. However, no sources of extended emission were detected in this image (Beam =  $6.15'' \times 4.87''$ ,  $43.23^\circ$ , RMS = 50 mJy beam $^{-1}$ ).

### 3.2 Known sources of diffuse emission

Of the 39 clusters in our sample 11 clusters are known in the literature to host radio halos and relics. The archival data we used was able to detect all the sources of extended emission in the clusters. Table 3 contains the list of these clusters as well as the flux density values of the sources as

estimated by this work compared to the literature. It should be noted that difference in flux density values for sources at the same frequency could be due to several reasons such as calibration or different sizes of the source taken during estimation.

#### 3.2.1 RX J0256.5+0006

The cluster is at a redshift of  $z = 0.36$  (Romer et al. 2000). Plionis et al. (2005) also give the X-ray luminosity of the cluster to be  $L_X = 2.84 \times 10^{44} \text{ erg s}^{-1}$  and a temperature of  $T_X = 5.6^{+0.7}_{-0.5}$ . Detailed *XMM-Newton* observations of the cluster by Majerowicz et al. (2004) revealed that this cluster shows two peaks in X-ray – one corresponding to the main cluster centre and another to its west – which suggests the cluster is in a merger state. A study of its dynamics showed that the merger is on-axis and the subcluster is roughly 20–30% of the main cluster by mass.

Recent GMRT 325 MHz and 610 MHz observations of the cluster (Knowles et al. 2016, 2019) revealed that the cluster does indeed host a faint radio halo.

#### 3.2.2 Abell 2163

A2163 is another massive cluster at a redshift of  $z = 0.203$  (Struble & Rood 1999). It has an X-ray luminosity of  $L_X = 34.37 \times 10^{44} \text{ erg s}^{-1}$  and a temperature of  $T_X = 13.4^{+0.45}_{-0.45} \text{ keV}$  (Planck Collaboration et al. 2011). The cluster hosts a  $\sim 3$  Mpc size radio halo (Herbig & Birkinshaw 1994; Feretti et al. 2001, 2004).

#### 3.2.3 Abell 2345

A2345 is an intermediate redshift ( $z = 0.176$  Struble & Rood (1999)) cluster with an X-ray luminosity of  $L_X = 6.47 \times 10^{44} \text{ erg s}^{-1}$ . The cluster contains double relics on opposite ends of the cluster (Bonafede et al. 2009).

#### 3.2.4 Abell 665

The cluster is at a redshift of  $z = 0.182$  (Struble & Rood 1999) and has an X-ray luminosity of  $L_X = 15.17 \times 10^{44} \text{ erg s}^{-1}$  (Böhringer et al. 2000). The temperature of this cluster has been estimated to be  $T_X = 7.5^{+0.2}_{-0.2} \text{ keV}$  (Maughan et al. 2008). This cluster is well known to host a 1.8 Mpc radio halo (Moffet & Birkinshaw 1989; Giovannini & Feretti 2000).

#### 3.2.5 Abell 0545

A545 has a redshift of  $z = 0.154$  (Struble & Rood 1999) and an X-ray luminosity of  $L_X = 8.37 \times 10^{44} \text{ erg s}^{-1}$  (Böhringer et al. 2004) with a temperature of  $T_X = 5.5^{+5.5}_{-2.1}$  (David et al. 1993). The X-ray structure of the cluster is disturbed (Buote & Tsai 1995; Buote 2001) and radio observations of the cluster (Bacchi et al. 2003) reveal the presence of a giant radio halo.

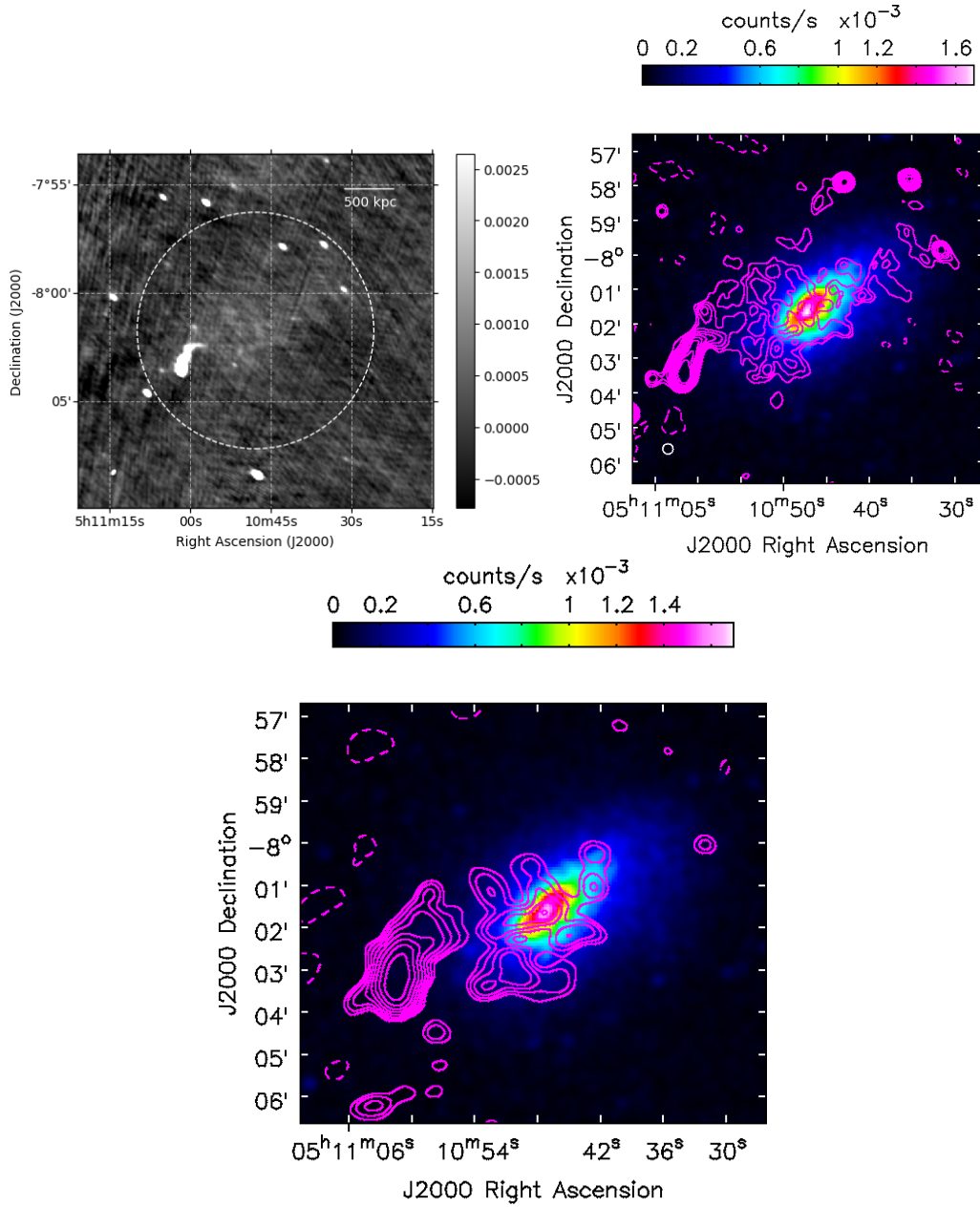


**Figure 3.** *Top Left:* Original output image from SPAM for the cluster RXC J0510.7-0801 at 325 MHz in grayscale. The resolution of the image is  $14.64'' \times 8.54''$ ,  $53.63^\circ$ . The dotted circle represents the  $R_{500}$  for the cluster as shown in the MCXC. The colour bar shows the flux density values in the image in Jy. *Top Right:* Radio contours for the cluster (magenta) overlaid on the *XMM-Newton* X-Ray image. The contours of the radio image start at  $3\sigma$ , where  $\sigma = 0.35$  mJy/beam and increase by  $\sqrt{2}$  afterwards. The resolution of the image is  $18'' \times 18''$ . The colour bar above shows the counts per second for the X-ray image. *Bottom:* Contours of the point source removed and smoothed image of the radio halo in the cluster overlaid on the X-ray image. The contours of the radio image start at  $3\sigma$  and increase by  $\sqrt{2}$  afterwards. The resolution of the image is  $48'' \times 44''$ ,  $45^\circ$ .

### 3.2.6 AS0780

AS0780 or RXCJ1459.4-1811 is a highly luminous cluster  $L_X = 22.94 \times 10^{44}$  erg  $s^{-1}$  found at a redshift of  $z = 0.236$  (Böhringer et al. 2004). Giacintucci et al. (2017) first claimed the cluster to host a mini-halo based on VLA 1.4 GHz observations. Using new GMRT and VLA observations Giacintucci et al. (2019) confirmed the presence of the mini-halo.

### 3.2.7 Abell 0907

A907 has a redshift of  $z = 0.153$  (Ebeling et al. 1996) and an X-ray luminosity of  $L_X = 7.59 \times 10^{44}$  erg  $s^{-1}$  (Böhringer et al. 2004). The gas temperature in the cluster has been estimated to be  $T_X = 5.3^{+0.1}_{-0.1}$  keV (Maughan et al. 2008). Giacintucci et al. (2019) claim that the cluster hosts a 65 kpc mini-halo.



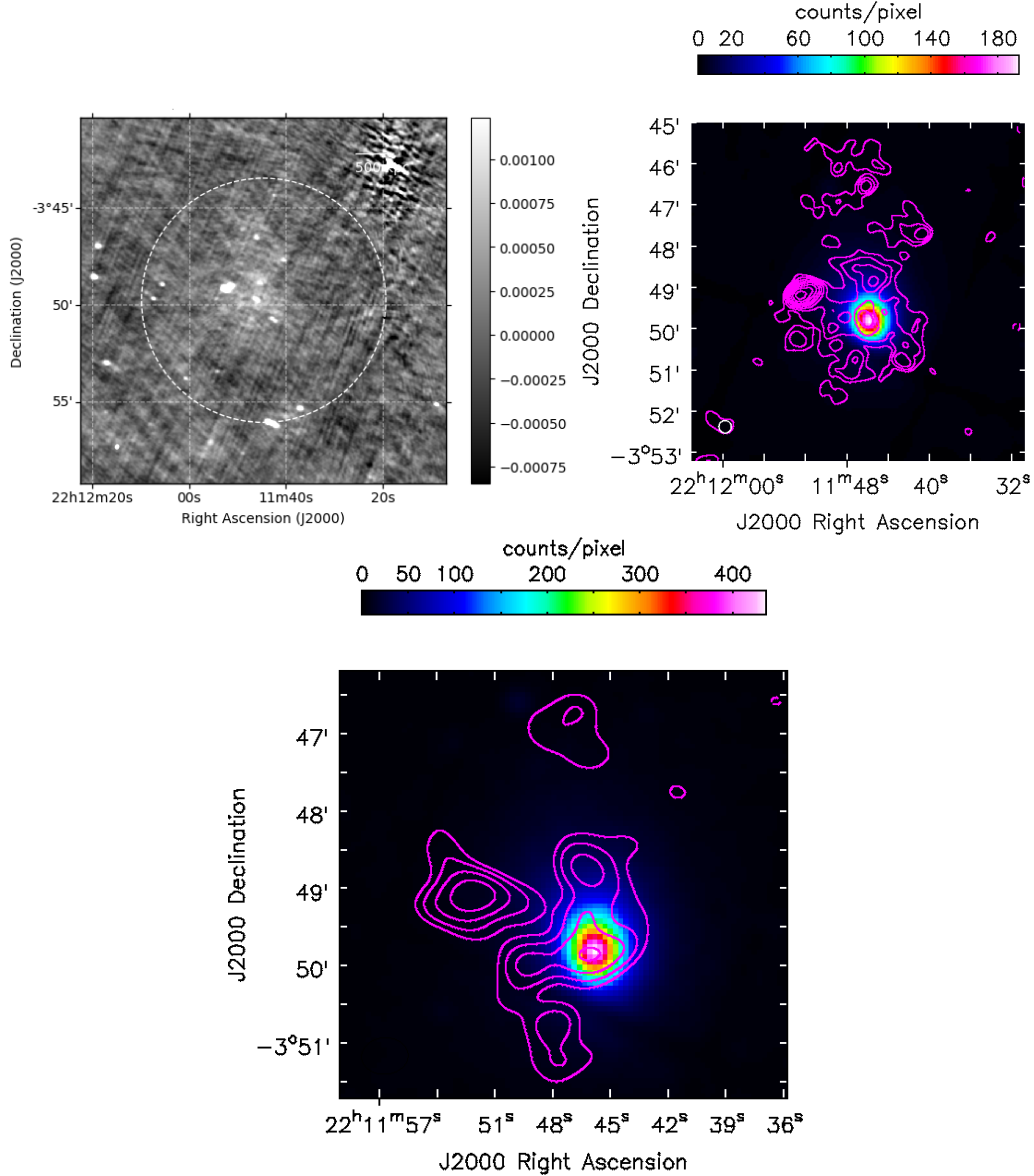


**Figure 4.** *Top Left:* Original output image from SPAM for the cluster RXC J2211.7-0349 at 325 MHz in grayscale. The resolution of the image is  $12.8'' \times 9.48''$ ,  $72^\circ$ . The dotted circle represents the  $R_{500}$  for the cluster as shown in the MCXC. The colour bar shows the flux density values in the image in Jy. *Top Right:* Radio contours for the cluster (magenta) overlaid on the *XMM-Newton* X-Ray image. The contours of the radio image start at  $3\sigma$  where  $\sigma = 0.4$  mJy/beam and increase by  $\sqrt{2}$  afterwards. The radio image has been convolved to  $18'' \times 18''$ . The colour bar above shows the counts per pixel for the X-ray image. *Bottom:* Contours of the point source removed and smoothed image of the radio halo in the cluster overlaid on the X-ray image. The contours of the radio image start at  $3\sigma$  and increase by  $\sqrt{2}$  afterwards. The resolution of the image is  $36'' \times 28''$ ,  $-86^\circ$ .

### 3.2.8 Abell 3444

A3444 is an intermediate redshift ( $z = 0.253$  Struble & Rood (1999)) highly luminous galaxy cluster ( $L_X = 18.11 \times 10^{44}$  erg  $s^{-1}$  Böhringer et al. (2004)) with a temperature of  $T_X = 5.6^{+0.24}_{-0.18}$  keV (Matsumoto et al. 2001). X-ray analysis by Lemonon et al. (1997) suggested that this is a cool-core cluster. The GRHS detected a possible extended emission which was confirmed to be a mini-halo recently by Giacintucci et al. (2019).

### 3.2.9 Abell 1300

A1300 is another highly luminous galaxy cluster ( $L_X = 19.23 \times 10^{44}$  erg  $s^{-1}$  Ebeling et al. (2010)) at a redshift of  $z = 0.307$  (Struble & Rood 1999). The cluster has a temperature of  $T_X = 7.75^{+0.31}_{-0.31}$  keV (Planck Collaboration et al. 2011). X-ray and optical observations (Lemonon et al. 1997) revealed that the cluster has a highly disturbed morphology and substructures. A radio halo and relic were first detected in this cluster by Reid et al. (1999). A low frequency follow-up observation with the GMRT was carried out by Giacintucci (2011) and Venturi et al. (2013) where the authors detected a faint bridge emission between the

**Table 3.** List of clusters with known diffuse emission. The subscript 0 represents images from this paper while the subscript 1 represents images from the reference paper given in the table. Some clusters contain a halo (H) as well as a relic (R) while others contain mini-halos (MH). A2345 is the only cluster with relics (East and West) and no central halo.

| Source           | $\nu_0$ (MHz) | $S_0$ (mJy)          | $\nu_1$ (MHz) | $S_1$ (mJy)                      | Reference   |
|------------------|---------------|----------------------|---------------|----------------------------------|---|
| RXC J0256.5+0006 | 610           | 30.99                | 610           | $6.9 \pm 0.7$                    | Knowles et al. (2016, 2019)                                     |
| A2163            | 325           | 1126.09 (H)/98 (R)   | 325           | $861 \pm 10$                     | Feretti et al. (2001, 2004)                                     |
| A2345            | 610           | 565.17(W)/408.48(E)  | 325           | $291 \pm 4$ (W)/ $188 \pm 3$ (E) | Bonafede et al. (2009)  |
| A665             | 240           | 462.58               | 325           | $197 \pm 6$                      | Giovannini & Feretti (2000); Feretti et al. (2004)              |
| A0545            | 325           | 624.9                | 1400          | $23 \pm 1$                       | Bacchi et al. (2003)  |
| AS0780           | 325           | 123.3 (MH)           | 610           | $34 \pm 2$                       | Giacintucci et al. (2019)                                       |
| A907             | 325           | 44.7 (MH)            | 610           | $34.9 \pm 5.6$                   | Giacintucci et al. (2019)                                       |
| A3444            | 325           | 21.36 (MH)           | 610           | $10.0 \pm 0.8$                   | Venturi et al. (2007); Giovannini et al. (2009)                 |
| A1300            | 325           | 207.67 (H)/90.59 (R) | 325           | $130 \pm 10$ (H)/ $75 \pm 6$ (R) | Reid et al. (1999); Venturi et al. (2013); Parekh et al. (2017) |
| RXC J1504.1-0248 | 325           | 220.8 (MH)           | 325           | $215 \pm 11$                     | Giacintucci et al. (2011b)                                      |
| RXC J1514.9-1523 | 325           | 139.5                | 325           | $102 \pm 9$                      | Giacintucci et al. (2011a)                                      |

halo and relic. Parekh et al. (2017) also performed a multi-frequency analysis of the cluster and confirmed the presence of this bridge as well as a second relic close to the halo.

### 3.2.10 RXC J1504.1-0248

The cluster has a redshift of  $z = 0.215$ . *Chandra* analysis of the cluster reveals the X-ray luminosity of the cluster to be  $L_X = 2.3 \times 10^{45}$  erg s $^{-1}$  (Böhringer et al. 2005). This study revealed the cluster to be the most luminous cluster in the southern sky at redshifts  $< 0.3$  with an extremely compact and dense core. High frequency radio observations by Mittal et al. (2009) show that the AGN in the cluster has a flat spectral index ( $\sim 0.29$ ) between 1.4 GHz and 4.86 GHz. Low frequency observations of the cluster at 327 MHz reveal the presence of a radio mini-halo nearly 140 kpc in size (Giacintucci et al. 2011a).

### 3.2.11 RXC J1514.9-1523

This cluster has a redshift of  $z = 0.223$  and an X-ray luminosity of  $L_X = 10.63 \times 10^{44}$  erg s $^{-1}$  (Böhringer et al. 2004). Radio observations of the cluster show that it contains an ultra steep spectrum radio halo (Giacintucci et al. 2011b).

## 4 DISCUSSION

Of the 39 clusters in the original sample we were able to image 38 clusters. The data for the cluster RXC J2014.8-2430 was too corrupted for us to properly image. The remaining 38 clusters were imaged with the SPAM software package. In the case of another cluster (RXJ1046.8-2535) no detailed X-ray information was available.

In Figure 5 we show the empirical relation between halo radio power at 1.4 GHz ( $P_{1.4}$ ) and the cluster X-ray luminosity ( $L_{500}$ ) and mass ( $M_{500}$ ). These studies of the relation between the radio properties of halos and the X-ray component of galaxy clusters can provide information about the origin of the synchrotron emission from the ICM. The radio power values for these plots were obtained from van Weeren et al. (2019) and references therein while the  $L_{500}$  and  $M_{500}$  values were obtained from Piffaretti et al. (2011). All the known halos from the literature are shown in black while all the upper limits from the literature are shown in red arrows. The best fit line was obtained following a method

**Table 4.** Estimated upper limits to radio halo emission in our sample. Col. 1: Cluster name, Col. 2: RMS in the central region, Col. 3: Frequency of image, Col. 4: Upper limit at this frequency, Col. 5: Log of the extrapolated radio power at 1.4 GHz

| Source           | RMS<br>[mJy beam $^{-1}$ ] | $\nu$<br>[MHz] | $S_{\nu}^{\text{UL}}$<br>[mJy] | $\log(P_{1.4}^{\text{UL}})$<br>[W Hz $^{-1}$ ] |
|------------------|----------------------------|----------------|--------------------------------|--|
| RX J1334.3+5030  | 0.14                       | 618            | 10.5                           | 24.86  |
| RX J1241.5+3250  | 0.165                      | 333            | 24.7                           | 24.38  |
| RX J0318.2-0301  | 0.154                      | 318            | 13.69                          | 23.65  |
| RX J1200.8-0327  | 0.2                        | 618            | 1.82                           | 22.58  |
| Abell 2345       | 0.577                      | 618            | 125.1                          | 24.62  |
| RX J1701.3+6414  | 0.284                      | 333            | 8.5                            | 24.07  |
| Abell 2390       | 0.9                        | 240            | 45.2                           | 23.92  |
| RXC J1308.5+5342 | 0.045                      | 618            | 6.00                           | 23.33  |
| RX J0847.1+3449  | 0.069                      | 618            | 11.09                          | 23.97  |
| RX J1120.1+4318  | 0.181                      | 333            | 36.2                           | 25.01  |
| Abell 1084       | 0.203                      | 318            | 101.6                          | 23.89  |
| Abell 1689       | 0.331                      | 317            | 66.12                          | 24.01  |
| Abell 0291       | 0.264                      | 317            | 57.23                          | 24.01  |
| RXC J1212.3-1816 | 0.148                      | 317            | 13.57                          | 23.7   |
| Abell 2104       | 0.449                      | 317            | 89.8                           | 23.97  |
| Abell 2485       | 0.338                      | 317            | 16.88                          | 23.71  |
| RXC J0437.1+0043 | 0.278                      | 317            | 55.5                           | 24.37  |
| Abell 0907       | 0.634                      | 317            | 422                            | 24.72  |
| Abell 2537       | 0.254                      | 317            | 50.8                           | 24.38  |

**Table 5.** Clusters with no upper limits calculated.

| Source          | $\nu$ (MHz) | Remarks                         |
|-----------------|-------------|---------------------------------|
| RX J0505.3-2849 | 325/610     | Bright source at cluster centre |
| A2597           | 610         | Bright source at cluster centre |
| RX J0426.1+1655 | 244/325/610 | Bright source at cluster centre |
| RX J2237.0+1516 | 325/610     | Bad image                       |
| A2319           | 325         | Bad image                       |
| A0400           | 325         | Bright source at cluster centre |
| A0901           | 325         | Bad image                       |

**Table 6.** Best fit values for  $L_X - P_{1.4}$  plot using four methods. The values correspond to a  $Y = AX + B$  model where  $X = \log(L_{500})$  and  $Y = \log(P_{1.4})$ . The values in bold are used in the plot.

| Method           | A             | $\sigma_A$    | B               | $\sigma_B$     |
|------------------|---------------|---------------|-----------------|----------------|
| <b>OLS (Y X)</b> | <b>1.8190</b> | <b>0.3126</b> | <b>-56.9956</b> | <b>14.0065</b> |
| OLS (X Y)        | 4.3765        | 0.9952        | -171.7180       | 44.7165        |
| bisector         | 2.6276        | 0.2825        | -93.2691        | 12.7114        |
| orthogonal       | 4.0723        | 0.9102        | -158.0726       | 40.9044        |

**Table 7.** Best fit values for  $M_X - P_{1.4}$  plot using four methods. The values correspond to a  $Y = AX + B$  model where  $X = \log(M_{500})$  and  $Y = \log(P_{1.4})$ . The values in bold are used in the plot.

| Method           | A             | $\sigma_A$    | B               | $\sigma_B$    |
|------------------|---------------|---------------|-----------------|---------------|
| <b>OLS (Y X)</b> | <b>3.0095</b> | <b>0.5969</b> | <b>-19.8687</b> | <b>8.8032</b> |
| OLS (X Y)        | 8.0905        | 2.1277        | -94.9471        | 31.4991       |
| bisector         | 4.4325        | 0.5095        | -40.8957        | 7.5512        |
| orthogonal       | 7.8851        | 2.0587        | -91.9113        | 30.4801       |

similar to Brunetti et al. (2009). Table 6 and 7 show the best fit values for the plots using four methods: Ordinary Least Squares (OLS) Y over X and X over Y, the bisector method and the orthogonal method. The authors recommend using the bisector method to estimate the best fit as suggested by Isobe et al. (1990) since it treats both variables symmetrically. However, in our case Piffaretti et al. (2011) do not provide error values for  $L_{500}$  and  $M_{500}$ . Therefore, using a method that requires errors on both variables will not be appropriate. So we use OLS (Y|X) for our best fit in the plots.

Recently, Cuciti et al. (2021) performed a similar analysis on a slightly larger cluster sample where they estimated the  $M_{500}$  values themselves and thus have errors on those variables. They provide best fits for both the Y|X method as well as the bisector method. Our best fit also agrees with their estimate of  $2.96 \pm 0.5$  for the slope using the Y|X method.

The green diamonds correspond to the two new detections from our sample. The flux density value of the halo at 325 MHz in our images was estimated from the uv-subtracted images shown in Fig. 3 and 4 and then scaled to 1.4 GHz (with k-correction applied) using an average halo spectral index of  $-1.3$  (Feretti et al. 2012). While RXC J0510.7-0801 fits the line very well, the detected halo in the massive cluster RXC J2211.7-0349 is almost an order of magnitude weaker in the  $M_{500} - P_{1.4}$  plot. Similar to Cuciti et al. (2018) who discovered two underluminous radio halos, the halo in this cluster could be the result of a minor merger or a result of the secondary model of halo formation due to hadronic collisions. It should be noted from Fig. 4 that the X-ray morphology of the cluster is much more relaxed and not that disturbed as compared to RXC J0510.7-0801 in Fig. 3. Thus, it is possible that the halo emission seen in the cluster is a remnant emission from early in the cluster’s history and is now comparatively much weaker after the merger is complete. Alternatively, the cluster could be in the earlier stages of a merger and the X-ray emission has not been disturbed yet.

For clusters in our sample where radio halos were not detected we tried to estimate upper limits (blue arrows in Fig. 5). The upper limits were estimated semi-automatically. The details of the process are described in detail in George et al. (2020). Briefly, for every cluster, a model halo image with an exponential profile (Bonafede et al. 2017) is created with a fixed position, redshift, size and flux density of the halo. This image is then Fourier transformed and added to the visibility file of the cluster on a per channel basis. The new visibility file is then imaged in CASA and the presence of a detection is checked automatically. This process is repeated for several flux densities until the halo is confirmed to

be “detected.” The code used to estimate halo upper limits is available [here](#)<sup>1</sup>.

Table 4 shows the estimated upper limits to halo flux densities at the corresponding reference frequencies as well as the extrapolated radio power upper limits at 1.4 GHz for other clusters in our sample. No limits are given for the following clusters: A2597, RX J0426.1+1655, RX J2237.0+1516, A2319, RXC J1308.5+5342, A0400, A0901 and A2485. We were unable to estimate the limits in these clusters for a few reasons as shown in Table 5. In some cases the quality of the image was extremely poor as a result of which proper estimates could not be made while in others the extent and brightness of the central BCG made estimation of any upper limit in the image extremely difficult. Note also that no upper limit has been estimated for the cluster RXJ1046.8-2535 since no relevant X-ray information is available for the cluster.

The GMRT Key Project on galaxy clusters was one of the first dedicated projects to make full use of the then untested capabilities of a low frequency telescope. The sample of clusters chosen to observe was a mix of clusters where halos had been previously detected at high frequencies (Giovannini et al. 1999) and others based on discussions with X-ray astronomers. The clusters spanned a wide range of redshifts and cluster mass so as to cover all possibilities of radio halo detection in a then burgeoning realm of radio astronomy.

As discussed in the previous section many of these clusters did turn out to host sources of extended emission when they were later observed after improving the telescope’s capabilities. In this paper we showed that with modern processing techniques such as direction dependant calibration found in SPAM it was still possible to detect the extended emission if not outright recover it. Blind surveys like this need to be conducted even in the future when new radio telescopes will be developed and their data needs to be carefully archived as they can lead to new discoveries when new processing techniques are discovered.

## 5 CONCLUSIONS

In this work we have analysed nearly two decade old archival GMRT observations of galaxy clusters using modern processing methods. The GMRT Key Project on galaxy clusters was undertaken within the first few years after the inauguration of the GMRT. The clusters chosen for observation were done so after careful consideration and deliberation with X-ray astronomers in order to make full use of the capabilities of the new telescope.

We analysed 38 galaxy clusters and were able to detect two new radio halos in the clusters RXC J0510.7-0801 and RXC J2211.7-0349. The former exhibits a highly disturbed X-ray morphology and is an example of a typical giant radio halo. It agrees fairly well with the observed correlation between cluster luminosity and radio halo power. RXC J2211.7-0349 on the other hand is a massive galaxy cluster that is quite relaxed and yet shows the presence of a weak radio halo. This cluster does not agree with the empirical relation very well. This could suggest that the halo emission is old and

<sup>1</sup> <https://github.com/lijotgeorge/upper-limit-calculator>

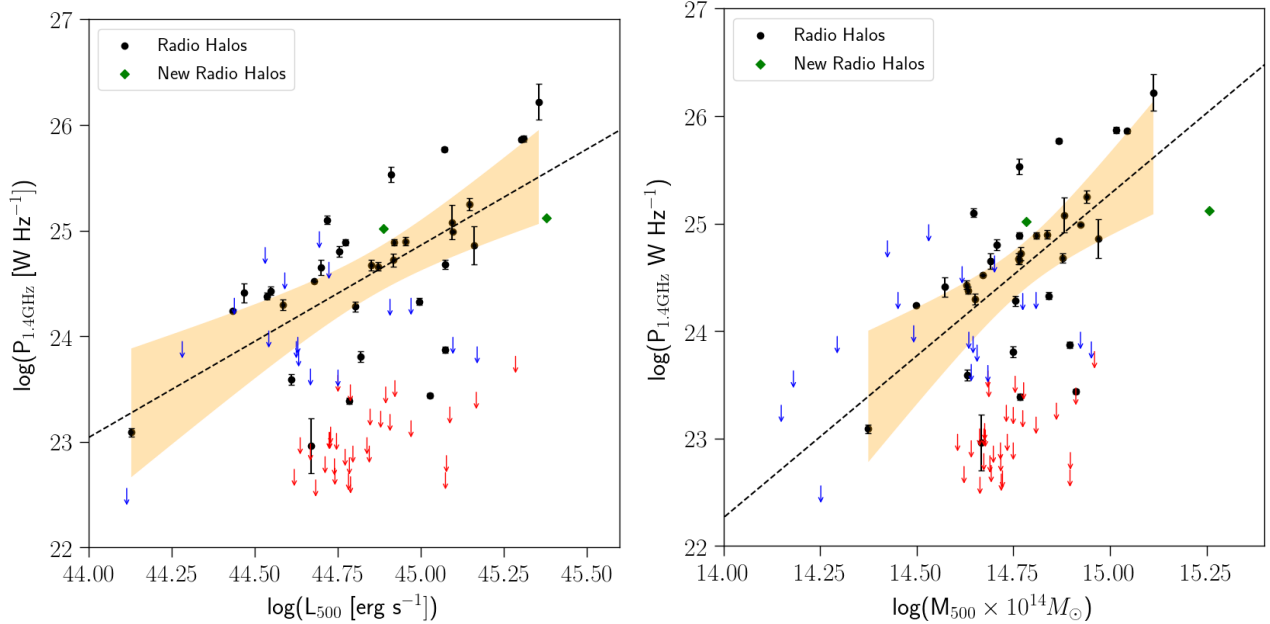


**Figure 5.** The empirical relations observed in galaxy clusters hosting radio halos between the X-Ray luminosity of the cluster and the radio power of the halo (*Left panel*) as well as the Mass of the cluster and the radio power of the halo (*Right panel*). All previously known detections in the literature are shown in black circles while upper limits are shown as red arrows. The two new halo detections in the paper are shown as green diamonds while the upper limits estimated are shown in blue arrows. The dashed line shows the best fit for each plot for all detections and the orange shaded region shows the  $2\sigma$  confidence intervals.

thus weaker now that there are no more sources generating ultra-relativistic electrons in the ICM. Or else the cluster is new and is in the very early stages of its merger or that the halo is a result of a minor merger or due to the secondary model of halo formation.

We also confirmed the presence of several halos and minihalos known in the literature from the archival data. Most of these clusters were later reobserved with the GMRT when the sensitivity of the telescope was much better and thus the data were of better quality. In the remaining 26 clusters we attempted to estimate upper limits to a possible radio halo emission. For this purpose we developed our own semi-automated upper limit calculator. We were able to estimate upper limits on 19 clusters in this manner. Upper limit estimation in the remaining clusters was not possible for various reasons.

Blind surveys like the GMRT Key Project are crucial when a new telescope becomes operational both to test the capabilities of the telescope as well as for the possibility of discovering new objects of scientific importance. This project also shows that even legacy data with all its shortcomings can still be useful when new analytical techniques and algorithms are developed and can lead to new discoveries.

## ACKNOWLEDGEMENTS

We thank the anonymous referee for providing their valuable comments to this paper which have helped improve it. We acknowledge the support of the Department of Atomic Energy, Government of India, under project no. 12-R&D-TFR-5.02-0700. We thank the staff of the GMRT that made these observations possible. GMRT is run by the National Cen-

tre for Radio Astrophysics of the Tata Institute of Fundamental Research. RK acknowledges support from the DST-INSPIRE Faculty Award of the Government of India. This research made use of Astropy,<sup>2</sup> a community-developed core Python package for Astronomy (Astropy Collaboration et al. 2013; Price-Whelan et al. 2018). This research made use of Astroquery, an astropy affiliated package that contains a collection of tools to access online Astronomical data (Ginsburg et al. 2019). This research has made use of the X-Rays Clusters Database (BAX) which is operated by the Laboratoire d’Astrophysique de Tarbes-Toulouse (LATT), under contract with the Centre National d’Etudes Spatiales (CNES). This research has made use of NASA’s Astrophysics Data System.

**Data Availability:** The data underlying this article were accessed from the GMRT Online Archive<sup>3</sup> (Project IDs: 01VKK01, 02VKK01, 03VKK01, 04VKK01, 05VKK01). The derived data generated in this research will be shared on reasonable request to the corresponding author.

## REFERENCES

- Ackermann M., Ajello M., Allafort A., Baldini L., et al., 2010, *ApJ*, **717**, L71  
 Aharonian F., Akhperjanian A. G., Anton G., Barres de Almeida U., et al., 2009a, *A&A*, **495**, 27  
 Aharonian F., Akhperjanian A. G., Anton G., Barres de Almeida U., et al., 2009b, *A&A*, **502**, 437

<sup>2</sup> <http://www.astropy.org>

<sup>3</sup> <https://naps.ncra.tifr.res.in/goa/data/search>



- Aleksić J., Antonelli L. A., Antoranz P., Backes M., et al., 2010, *ApJ*, **710**, 634
- Allen S. W., Schmidt R. W., Fabian A. C., Ebeling H., 2003, *MNRAS*, **342**, 287
- Arnaud M., Pratt G. W., Piffaretti R., Böhringer H., Croston J. H., Pointecouteau E., 2010, *A&A*, **517**, A92
- Astropy Collaboration et al., 2013, *A&A*, **558**, A33
- Bacchi M., Feretti L., Giovannini G., Govoni F., 2003, *A&A*, **400**, 465
- Baldi A., Etti S., Mazzotta P., Tozzi P., Borgani S., 2007, *ApJ*, **666**, 835
- Blandford R., Eichler D., 1987, *Phys. Rep.*, **154**, 1
- Blasi P., Colafrancesco S., 1999, *Astroparticle Physics*, **12**, 169
- Böhringer H., et al., 2000, *ApJS*, **129**, 435
- Böhringer H., et al., 2004, *A&A*, **425**, 367
- Böhringer H., Burwitz V., Zhang Y.-Y., Schuecker P., Nowak N., 2005, *ApJ*, **633**, 148
- Bonafede A., Giovannini G., Feretti L., Govoni F., Murgia M., 2009, *A&A*, **494**, 429
- Bonafede A., et al., 2017, *Monthly Notices of the Royal Astronomical Society*, **470**, 3465
- Bowman J. D., Cairns I., Kaplan D. L., Murphy T., et al., 2013, *Publ. Astron. Soc. Australia*, **30**, 31
- Brunetti G., Jones T. W., 2014, *International Journal of Modern Physics D*, **23**, 30007
- Brunetti G., Lazarian A., 2011, *MNRAS*, **410**, 127
- Brunetti G., Setti G., Feretti L., Giovannini G., 2001, *MNRAS*, **320**, 365
- Brunetti G., Venturi T., Dallacasa D., Cassano R., Dolag K., Giacintucci S., Setti G., 2007, *ApJ*, **670**, L5
- Brunetti G., Cassano R., Dolag K., Setti G., 2009, *A&A*, **507**, 661
- Buote D. A., 2001, *ApJ*, **553**, L15
- Buote D. A., Tsai J. C., 1995, *ApJ*, **452**, 522
- Burke D. J., Collins C. A., Sharples R. M., Romer A. K., Nichol R. C., 2003, *MNRAS*, **341**, 1093
- Cassano R., Etti S., Giacintucci S., Brunetti G., Markevitch M., Venturi T., Gitti M., 2010, *ApJ*, **721**, L82
- Cavagnolo K. W., Donahue M., Voit G. M., Sun M., 2008, *ApJ*, **682**, 821
- Cotton B., 2013, *Obit: Radio Astronomy Data Handling* (ascl:1307.008)
- Crudace R., et al., 2002, *ApJS*, **140**, 239
- Cuciti V., Brunetti G., van Weeren R., Bonafede A., Dallacasa D., Cassano R., Venturi T., Kale R., 2018, *A&A*, **609**, A61
- Cuciti V., et al., 2021, arXiv e-prints, p. [arXiv:2101.01640](https://arxiv.org/abs/2101.01640)
- Dahle H., Kaiser N., Irgens R. J., Lilje P. B., Maddox S. J., 2002, *ApJS*, **139**, 313
- David L. P., Slyz A., Jones C., Forman W., Vrtilek S. D., Arnaud K. A., 1993, *ApJ*, **412**, 479
- De Grandi S., et al., 1999, *ApJ*, **514**, 148
- Dennison B., 1980, *ApJ*, **239**, L93
- Dewdney P., Turner W., Millenaar R., McCool R., Lazio J., Cornwell T. J., 2013, *SKA1 System Baseline Design*, Document number SKA-TEL-SKO-DD-001
- Dietrich J. P., Erben T., Lamer G., Schneider P., Schwobe A., Hartlap J., Maturi M., 2007, *A&A*, **470**, 821
- Ebeling H., Voges W., Böhringer H., Edge A. C., Huchra J. P., Briel U. G., 1996, *MNRAS*, **281**, 799
- Ebeling H., Edge A. C., Allen S. W., Crawford C. S., Fabian A. C., Huchra J. P., 2000, *MNRAS*, **318**, 333
- Ebeling H., Edge A. C., Mantz A., Barrett E., Henry J. P., Ma C. J., van Speybroeck L., 2010, *MNRAS*, **407**, 83
- Ehlert S., Ulmer M. P., 2009, *A&A*, **503**, 35
- Ensslin T. A., Biermann P. L., Klein U., Kohle S., 1998, *A&A*, **332**, 395
- Etti S., Balestra I., 2009, *A&A*, **496**, 343
- Farnsworth D., Rudnick L., Brown S., Brunetti G., 2013, *ApJ*, **779**, 189
- Feretti L., 2000, ArXiv Astrophysics e-prints,
- Feretti L., Giovannini G., Böhringer H., 1997, *New Astron.*, **2**, 501
- Feretti L., Fusco-Femiano R., Giovannini G., Govoni F., 2001, *A&A*, **373**, 106
- Feretti L., Orrù E., Brunetti G., Giovannini G., Kassim N., Setti G., 2004, *A&A*, **423**, 111
- Feretti L., Schuecker P., Böhringer H., Govoni F., Giovannini G., 2005, *A&A*, **444**, 157
- Feretti L., Giovannini G., Govoni F., Murgia M., 2012, *A&ARv*, **20**, 54
- George L. T., Kale R., Wadadekar Y., 2020, arXiv e-prints, p. [arXiv:2012.03008](https://arxiv.org/abs/2012.03008)
- Giacintucci S., 2011, *Mem. Soc. Astron. Italiana*, **82**, 541
- Giacintucci S., Markevitch M., Brunetti G., Cassano R., Venturi T., 2011a, *A&A*, **525**, L10
- Giacintucci S., Dallacasa D., Venturi T., Brunetti G., Cassano R., Markevitch M., Athreya R. M., 2011b, *A&A*, **534**, A57
- Giacintucci S., Markevitch M., Cassano R., Venturi T., Clarke T. E., Brunetti G., 2017, *ApJ*, **841**, 71
- Giacintucci S., Markevitch M., Cassano R., Venturi T., Clarke T. E., Kale R., Cuciti V., 2019, *ApJ*, **880**, 70
- Ginsburg A., et al., 2019, *AJ*, **157**, 98
- Giovannini G., Feretti L., 2000, *New Astron.*, **5**, 335
- Giovannini G., Tordi M., Feretti L., 1999, *New Astron.*, **4**, 141
- Giovannini G., Bonafede A., Feretti L., Govoni F., Murgia M., Ferrari F., Monti G., 2009, *A&A*, **507**, 1257
- Govoni F., Feretti L., Giovannini G., Böhringer H., Reiprich T. H., Murgia M., 2001, *A&A*, **376**, 803
- Herbig T., Birkinshaw M., 1994, in *American Astronomical Society Meeting Abstracts*. p. 53.07
- Hudson D. S., Mittal R., Reiprich T. H., Nulsen P. E. J., Anderson H., Sarazin C. L., 2010, *A&A*, **513**, A37
- Ikebe Y., Reiprich T. H., Böhringer H., Tanaka Y., Kitayama T., 2002, *A&A*, **383**, 773
- Intema H. T., 2014, in *Astronomical Society of India Conference Series*. ([arXiv:1402.4889](https://arxiv.org/abs/1402.4889))
- Intema H. T., Jagannathan P., Mooley K. P., Frail D. A., 2017, *A&A*, **598**, A78
- Isobe T., Feigelson E. D., Akritas M. G., Babu G. J., 1990, *ApJ*, **364**, 104
- Johnston S., Feain I. J., Gupta N., 2009, in Saikia D. J., Green D. A., Gupta Y., Venturi T., eds, *Astronomical Society of the Pacific Conference Series Vol. 407, The Low-Frequency Radio Universe*. p. 446 ([arXiv:0903.4011](https://arxiv.org/abs/0903.4011))
- Jones F. C., Ellison D. C., 1991, *Space Sci. Rev.*, **58**, 259
- Kale R., Venturi T., Giacintucci S., Dallacasa D., Cassano R., Brunetti G., Macario G., Athreya R., 2013, *A&A*, **557**, A99
- Kale R., et al., 2015, *A&A*, **579**, A92
- Kettenis M., Sipior M., 2012, *ParselTongue: AIPS Python Interface* (ascl:1208.020)
- Knowles K., et al., 2016, *MNRAS*, **459**, 4240
- Knowles K., et al., 2019, *MNRAS*, **486**, 1332
- Kotov O., Vikhlinin A., 2005, *ApJ*, **633**, 781
- Lemonon L., Pierre M., Hunstead R., Reid A., Mellier Y., Böhringer H., 1997, *A&A*, **326**, 34
- Liang H., Hunstead R. W., Birkinshaw M., Andreani P., 2000, *ApJ*, **544**, 686
- Lonsdale C. J., Cappallo R. J., Morales M. F., Briggs F. H., et al., 2009, *IEEE Proceedings*, **97**, 1497
- Lumb D. H., et al., 2004, *A&A*, **420**, 853
- Majerowicz S., Arnaud M., Neumann D. M., 2003, in Bowyer S., Hwang C.-Y., eds, *Astronomical Society of the Pacific Conference Series Vol. 301, Matter and Energy in Clusters of Galaxies*. p. 531 ([arXiv:astro-ph/0207232](https://arxiv.org/abs/astro-ph/0207232))
- Majerowicz S., Neumann D. M., Romer A. K., Nichol R. C., Burke D. J., Collins C. A., 2004, *A&A*, **425**, 15

- Matsumoto H., Pierre M., Tsuru T. G., Davis D. S., 2001, *A&A*, **374**, 28
- Maughan B. J., Jones C., Forman W., Van Speybroeck L., 2008, *ApJS*, **174**, 117
- McMullin J. P., Waters B., Schiebel D., Young W., Golap K., 2007, in Shaw R. A., Hill F., Bell D. J., eds, *Astronomical Society of the Pacific Conference Series Vol. 376, Astronomical Data Analysis Software and Systems XVI*. p. 127
- Mittal R., Hudson D. S., Reiprich T. H., Clarke T., 2009, *A&A*, **501**, 835
- Moffet A. T., Birkinshaw M., 1989, *AJ*, **98**, 1148
- Mullis C. R., et al., 2003, *ApJ*, **594**, 154
- Parekh V., Dwarakanath K. S., Kale R., Intema H., 2017, *MNRAS*, **464**, 2752
- Petrosian V., 2001, *ApJ*, **557**, 560
- Pfrommer C., Enßlin T. A., 2004, *A&A*, **413**, 17
- Pierre M., Böhringer H., Ebeling H., Voges W., Schuecker P., Cruddace R., MacGillivray H., 1994, *A&A*, **290**, 725
- Piffaretti R., Arnaud M., Pratt G. W., Pointecouteau E., Melin J.-B., 2011, *A&A*, **534**, A109
- Pimblet K. A., Smail I., Edge A. C., O’Hely E., Couch W. J., Zabludoff A. I., 2006, *MNRAS*, **366**, 645
- Planck Collaboration et al., 2011, *A&A*, **536**, A11
- Plionis M., Basilakos S., Georgantopoulos I., Georgakakis A., 2005, *ApJ*, **622**, L17
- Pratt G. W., Böhringer H., Croston J. H., Arnaud M., Borgani S., Finoguenov A., Temple R. F., 2007, *A&A*, **461**, 71
- Pratt G. W., Croston J. H., Arnaud M., Böhringer H., 2009, *A&A*, **498**, 361
- Price-Whelan A. M., et al., 2018, *AJ*, **156**, 123
- Reid A. D., Hunstead R. W., Lemonon L., Pierre M. M., 1999, *MNRAS*, **302**, 571
- Reiprich T. H., Böhringer H., 2002, *ApJ*, **567**, 716
- Romer A. K., et al., 2000, *ApJS*, **126**, 209
- Rossetti M., et al., 2016, *MNRAS*, **457**, 4515
- Schindler S., 2000, *A&AS*, **142**, 433
- Sommer M. W., Basu K., Intema H., Pacaud F., Bonafede A., Babul A., Bertoldi F., 2017, *MNRAS*, **466**, 996
- Storm E., Jeltema T. E., Rudnick L., 2015, *MNRAS*, **448**, 2495
- Struble M. F., Rood H. J., 1999, *ApJS*, **125**, 35
- Tingay S. J., Goeke R., Bowman J. D., Emrich D., et al., 2013, *Publ. Astron. Soc. Australia*, **30**, 7
- Truemper J., 1993, *Science*, **260**, 1769
- Vazza F., Brüggén M., 2014, *MNRAS*, **437**, 2291
- Vazza F., Eckert D., Brüggén M., Huber B., 2015, *MNRAS*, **451**, 2198
- Vazza F., Brüggén M., Wittor D., Gheller C., Eckert D., Stubbe M., 2016, *MNRAS*, **459**, 70
- Venturi T., Giacintucci S., Brunetti G., Cassano R., Bardelli S., Dallacasa D., Setti G., 2007, *A&A*, **463**, 937
- Venturi T., Giacintucci S., Dallacasa D., Cassano R., Brunetti G., Bardelli S., Setti G., 2008, *A&A*, **484**, 327
- Venturi T., Giacintucci S., Dallacasa D., Cassano R., Brunetti G., Macario G., Athreya R., 2013, *A&A*, **551**, A24
- Vikhlinin A., McNamara B. R., Forman W., Jones C., Quintana H., Hornstrup A., 1998, *ApJ*, **502**, 558
- Vikhlinin A., et al., 2009, *ApJ*, **692**, 1033
- Weißmann A., Böhringer H., Šuhada R., Ameglio S., 2013, *A&A*, **549**, A19
- Wells D. C., 1985, in di Gesu V., Scarsi L., Crane P., Friedman J. H., Levaldi S., eds, *Data Analysis in Astronomy*. p. 195
- Wen Z. L., Han J. L., Liu F. S., 2012, *ApJS*, **199**, 34
- Zhang Y.-Y., Böhringer H., Finoguenov A., Ikebe Y., Matsushita K., Schuecker P., Guzzo L., Collins C. A., 2006, *A&A*, **456**, 55
- Zhang Y.-Y., Finoguenov A., Böhringer H., Kneib J.-P., Smith G. P., Kneissl R., Okabe N., Dahle H., 2008, *A&A*, **482**, 451
- van Haarlem M. P., Wise M. W., Gunst A. W., Heald G., et al., 2013, *A&A*, **556**, A2
- van Weeren R. J., de Gasperin F., Akamatsu H., Brüggén M., Feretti L., Kang H., Stroe A., Zandanel F., 2019, *Space Sci. Rev.*, **215**, 16

## APPENDIX A: OTHER CLUSTERS

### A1 RX J1334.3+5030

At a redshift of  $z = 0.62$  (Romer et al. 2000) this cluster has the highest redshift in the sample. It has an X-ray luminosity of  $L_X = 3.9 \times 10^{44}$  erg s $^{-1}$  (Lumb et al. 2004). The temperature of the cluster was estimated by Kotov & Vikhlinin (2005) to be  $T_X = 4.6^{+0.4}_{-0.3}$  and  $M_{500} = 2.73^{+0.45}_{-0.3} \times 10^{14} M_\odot$ .

### A2 RX J0505.3-2849

This cluster is at a redshift  $z = 0.509$  (Burke et al. 2003) and has an X-ray luminosity of  $L_X = 1.1 \times 10^{44}$  erg s $^{-1}$  and is at a temperature of  $T_X = 2.5^{+0.3}_{-0.3}$  keV (Lumb et al. 2004). X-ray observations of the cluster with the *XMM-Newton* show the presence of two peaks one of which has been claimed to be due to confusion with a double point source (Dietrich et al. 2007).

### A3 RX J1241.5+3250

This cluster has a redshift of  $z = 0.39$  and an X-ray luminosity of  $L_X = 4.8 \times 10^{44}$  erg s $^{-1}$  (Romer et al. 2000). The temperature of the cluster was estimated to be  $T_X = 6$  keV.

### A4 RX J0318.2-0301

The cluster has a redshift  $z = 0.37$  (Romer et al. 2000). X-ray analysis of the clusters give the luminosity of the cluster to be  $L_X = 1.74 \times 10^{44}$  erg s $^{-1}$  (Burke et al. 2003) and a temperature of  $T_X = 5.7^{+0.3}_{-0.3}$  keV (Ehlert & Ulmer 2009).

### A5 RX J1200.8-0327

This cluster has a redshift of  $z = 0.396$  (Mullis et al. 2003) and an X-ray luminosity of  $L_X = 2.02 \times 10^{44}$  erg s $^{-1}$  (Vikhlinin et al. 1998). The X-ray distribution of the cluster is spherically symmetric and it seems to be in a relaxed state with a global temperature of  $T_X = 5.1^{+0.7}_{-0.5}$  keV (Majerowicz et al. 2004).

### A6 Abell 2597

A2597 is a nearby cool-core cluster with a redshift of  $z = 0.085$  (Struble & Rood 1999). It has an X-ray luminosity of  $L_X = 6.62 \times 10^{44}$  erg s $^{-1}$  (Reiprich & Böhringer 2002) and a temperature of  $T_X = 4.05$  keV (Hudson et al. 2010). X-ray observations show the presence of cold, accretion flow in the cluster towards the central supermassive black hole.



**A7 RX J0426.1+1655**

The cluster has a redshift of  $z = 0.38$  and an X-ray luminosity of  $L_X = 4.94 \times 10^{44}$  erg s<sup>-1</sup> (Romer et al. 2000). The temperature of the cluster has been estimated to be  $T_X = 5.4_{0.4}^{0.4}$  keV (Ehlert & Ulmer 2009).

**A8 RX J2237.0-1516**

This cluster is an intermediate redshift ( $z = 0.299$ ) cluster with a weak X-ray luminosity  $L_X = 2.18 \times 10^{44}$  erg s<sup>-1</sup> (Romer et al. 2000). The mean temperature of the cluster was estimated to be  $T_X = 3.0 \pm_{0.5}^{0.5}$  keV (Majerowicz et al. 2004). *XMM-Newton* analysis do not reveal any structure in the X-ray distribution (Majerowicz et al. 2003).

**A9 Abell 2319**

A2319 is a highly luminous nearby cluster with a redshift of  $z = 0.056$  (Struble & Rood 1999) and an X-ray luminosity of  $L_X = 15.78 \times 10^{44}$  erg s<sup>-1</sup> (Reiprich & Böhringer 2002). It has a temperature of  $T_X = 8.84_{0.14}^{0.18}$  keV (Ikebe et al. 2002). VLA and GBT observations of the cluster reveal the presence of a  $\sim 2$  Mpc size radio halo with a complex morphology (Feretti et al. 1997; Farnsworth et al. 2013; Storm et al. 2015).

**A10 RX J1701.3+6414**

This is high redshift cluster ( $z = 0.453$ ) with an X-ray luminosity of  $L_X = 3.4 \times 10^{44}$  erg s<sup>-1</sup> (Lumb et al. 2004) and a temperature of  $T_X = 4.36_{0.46}^{0.46}$  keV (Vikhlinin et al. 2009).

**A11 Abell 2390**

This massive cluster has a redshift of  $z = 0.228$  (Struble & Rood 1999) and an X-ray luminosity of  $L_X = 25.09 \times 10^{44}$  erg s<sup>-1</sup> (Allen et al. 2003) and a gas temperature of  $T_X = 8.89_{0.24}^{0.24}$  keV (Planck Collaboration et al. 2011). The extended emission in this cool-core cluster was initially identified as a mini-halo (Bacchi et al. 2003). Later observations revealed however, that the emission was much larger than previously measured and the source is in fact a radio halo with a steep spectrum (Sommer et al. 2017).

**A12 RXC J1308.5+5342**

This cluster has a redshift of  $z = 0.33$  and an X-ray luminosity of  $L_X = 1.53 \times 10^{44}$  erg s<sup>-1</sup> (Lumb et al. 2004). The temperature of the cluster is  $T_X = 4.36_{0.38}^{0.38}$  keV (Ettori & Balestra 2009).

**A13 RX J0847.1+3449**

This is a high redshift cluster ( $z = 0.56$  Vikhlinin et al. (1998)) and is not very luminous ( $L_X = 1.59 \times 10^{44}$  erg s<sup>-1</sup> Lumb et al. (2004)). The X-ray temperature of the cluster gas has also been estimated by Lumb et al. (2004) to be  $T_X = 3.62_{0.51}^{0.58}$  keV.

**A14 Abell 0400**

A400 is a low redshift cluster ( $z = 0.024$  Struble & Rood (1999)) with a very low X-ray luminosity of  $L_X = 0.71 \times 10^{44}$  erg s<sup>-1</sup> and a temperature of  $T_X = 2.43_{0.7}^{0.8}$  keV. GBT observations by Farnsworth et al. (2013) were not able to detect any source of extended emission as the central cluster is dominated by emission due to the tailed radio galaxy 3C275.

**A15 RX J1120.1+4318**

This is another high redshift cluster ( $z = 0.6$  Romer et al. (2000)). Lumb et al. (2004) estimated the X-ray luminosity of the cluster as  $L_X = 6.07 \times 10^{44}$  erg s<sup>-1</sup> and temperature to be  $T_X = 5.45_{0.3}^{0.3}$  keV.

**A16 Abell 1084**

A1084 has a redshift of  $z = 0.132$  (Pimblet et al. 2006). The cluster has an X-ray luminosity of  $L_X = 6.82 \times 10^{44}$  erg s<sup>-1</sup> (Böhringer et al. 2004) and a temperature of  $T_X = 3.56_{0.5}^{0.5}$  keV (Pratt et al. 2007). Visual inspection of the ROSAT image for this cluster showed that it has an irregular morphology (Pimblet et al. 2006).

**A17 Abell 1689**

A1689 is a highly luminous galaxy cluster ( $L_X = 19.88 \times 10^{44}$ ) erg s<sup>-1</sup> (Reiprich & Böhringer 2002) at a redshift of  $z = 0.183$  (Struble & Rood 1999). It has an X-ray temperature of  $T_X = 8.17_{0.12}^{0.12}$  keV (Planck Collaboration et al. 2011).

**A18 RXC J2014.8-2430**

This cluster has a redshift of  $z = 0.161$  and an X-ray luminosity of  $L_X = 15.13 \times 10^{44}$  erg s<sup>-1</sup> (Böhringer et al. 2004). The temperature of the cluster is  $T_X = 4.78_{0.5}^{0.5}$  keV (Pratt et al. 2009). A morphological analysis of the cluster (Weißmann et al. 2013) revealed the cluster to be in a relaxed state.

**A19 Abell 0901**

A901 is at a redshift of  $z = 0.17$  (Schindler 2000) and an X-ray luminosity of  $L_X = 10.73 \times 10^{44}$  erg s<sup>-1</sup> (Böhringer et al. 2004). It also has a temperature of  $T_X = 3.2_{0.2}^{0.2}$  keV (Zhang et al. 2008). The X-ray analysis by Schindler (2000) revealed the cluster to have a relaxed morphology.

**A20 Abell 0291**

A0291 is at a redshift of  $z = 0.197$  (Struble & Rood 1999) and has an X-ray luminosity of  $L_X = 6.81 \times 10^{44}$  erg s<sup>-1</sup> (Böhringer et al. 2004).

**A21 RXC J1212.3-1816**

This cluster has a redshift of  $z = 0.269$  and an X-ray luminosity of  $L_X = 9.17 \times 10^{44}$  erg s<sup>-1</sup> (Böhringer et al. 2004). The cluster was observed by Kale et al. (2013, 2015) but no sources of extended emission were found.

**A22 RX J1046.8-2535**

The cluster is at a redshift of  $z = 0.2426$  (Pierre et al. 1994). Not much is known about this cluster either in X-ray or radio.

**A23 Abell 2104**

This cluster has a redshift of  $z = 0.153$  (Pimblet et al. 2006). The X-ray luminosity of the cluster is  $L_X = 7.26 \times 10^{44}$  erg s<sup>-1</sup> (Böhringer et al. 2004) and a temperature of  $T_X = 6.76_{0.19}^{0.19}$  keV (Baldi et al. 2007).

**A24 Abell 2485**

This cluster is at a redshift  $z = 0.247$  and has an X-ray luminosity of  $L_X = 7.73 \times 10^{44}$  erg s<sup>-1</sup> (Böhringer et al. 2004). Kale et al. (2013) did not find any source of diffuse emission in the cluster.

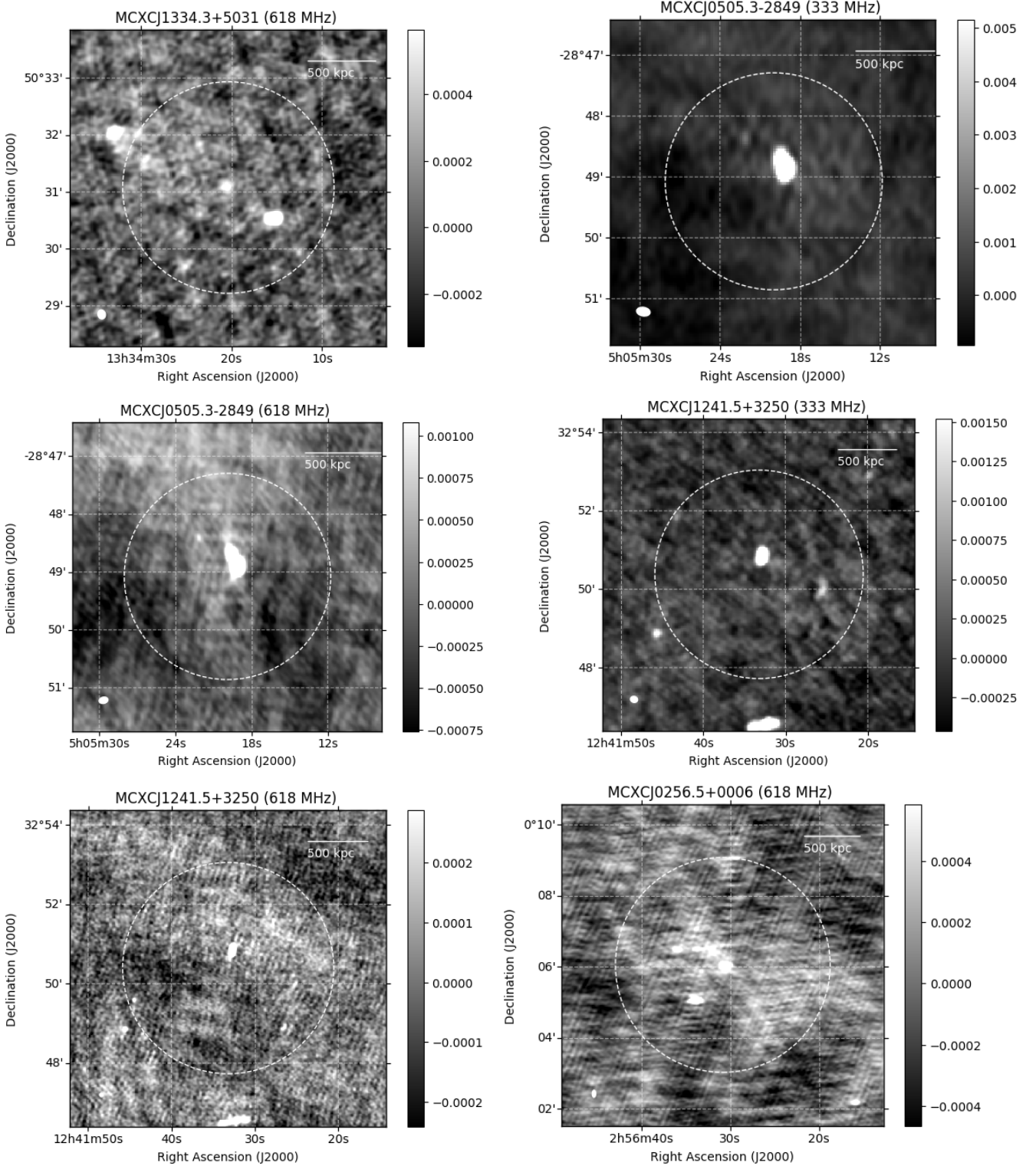
**A25 RXC J0437.1+0043**

This cool core cluster is at a redshift of  $z = 0.285$  and has an X-ray luminosity of  $L_X = 11.91 \times 10^{44}$  erg s<sup>-1</sup> (Ebeling et al. 2000). Zhang et al. (2006) estimate the temperature of the cluster to be  $T_X = 5.1_{0.3}^{0.3}$  keV and the mass of the cluster to be  $M_X = 6.1 \pm 2.2 \times 10^{14} M_\odot$ . VLA observations of the cluster (Feretti et al. 2005) did not reveal the presence of any diffuse emission in the cluster.

**A26 Abell 2537**

A2537 is a hot ( $T_X = 8.4_{0.68}^{0.76}$  keV Cavagnolo et al. (2008)), highly luminous ( $L_X = 14.78 \times 10^{44}$  erg s<sup>-1</sup> Cruddace et al. (2002)) with a redshift of  $z = 0.295$  (Dahle et al. 2002). The cluster was observed as part of the GRHS (Venturi et al. 2007) and the authors did not detect any source of extended emission in the cluster. The authors in their observations mention the emission in the cluster to be dominated by a tailed radio galaxy near the centre which has been detected by our analysis as well.

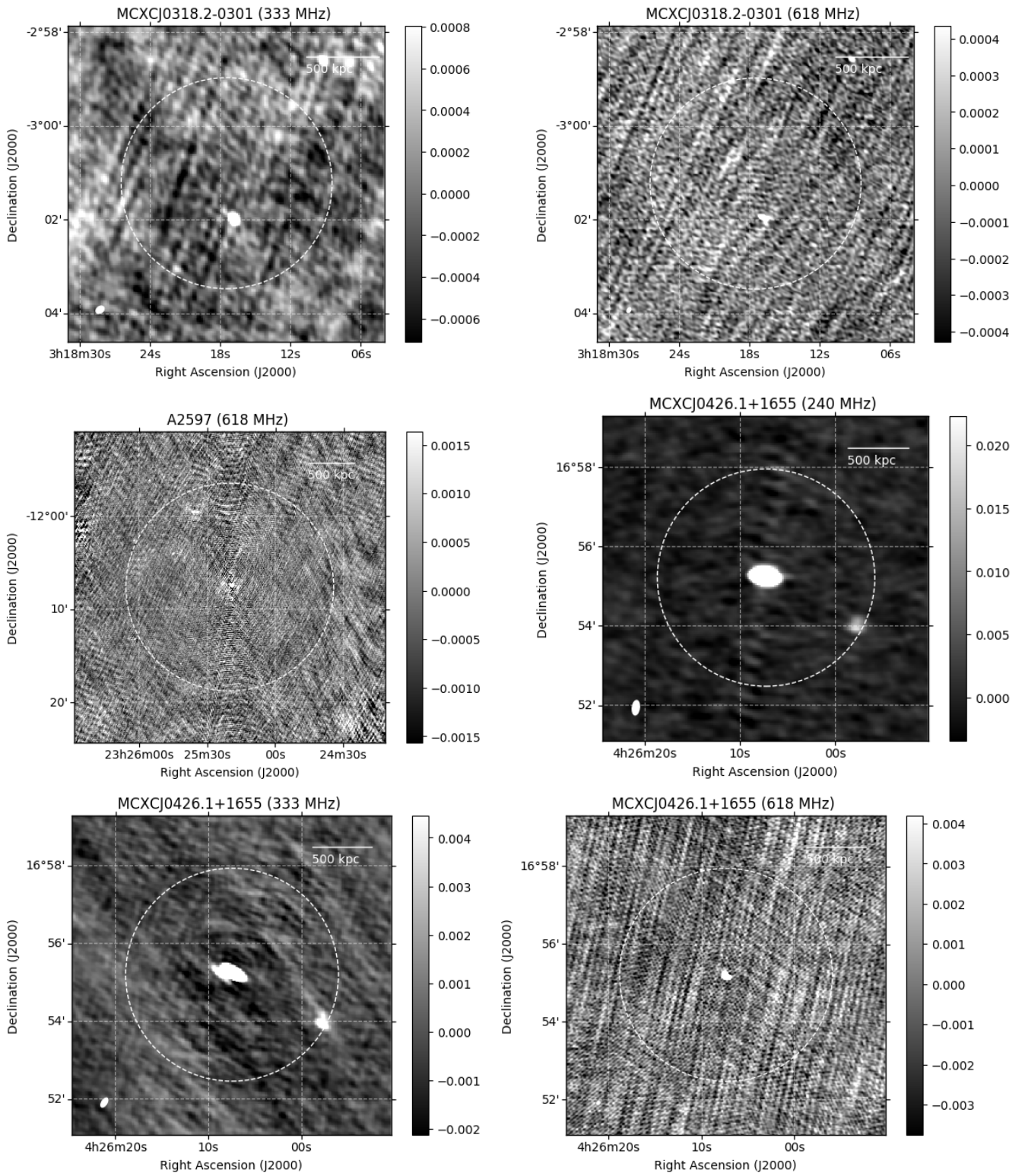
This paper has been typeset from a  $\text{\TeX}/\text{\LaTeX}$  file prepared by the author.



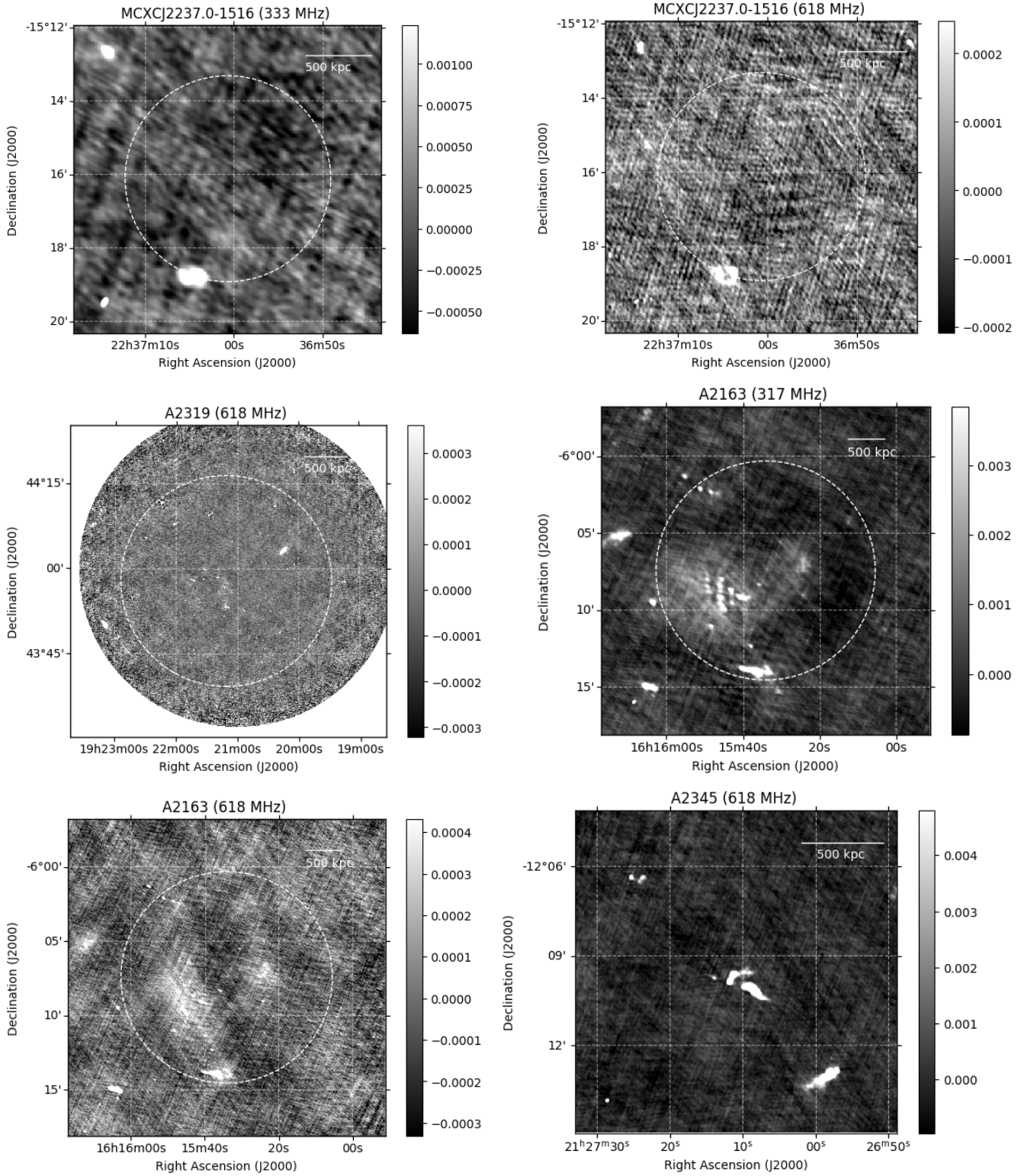
(a) Radio images

**Figure A1.** Radio images for the clusters in our sample. Dashed circles represent  $R_{500}$  as given by MCXC. The units of the colourbar are in Jansky/beam. These images were created using astropy with interval levels determined automatically for each image using the PercentileInterval option. By default, 99% of the pixels were used to estimate the limits with the exceptions being RXC J0847.1+3449 and RX J1046.8-2535 where 98% of the pixels were used.



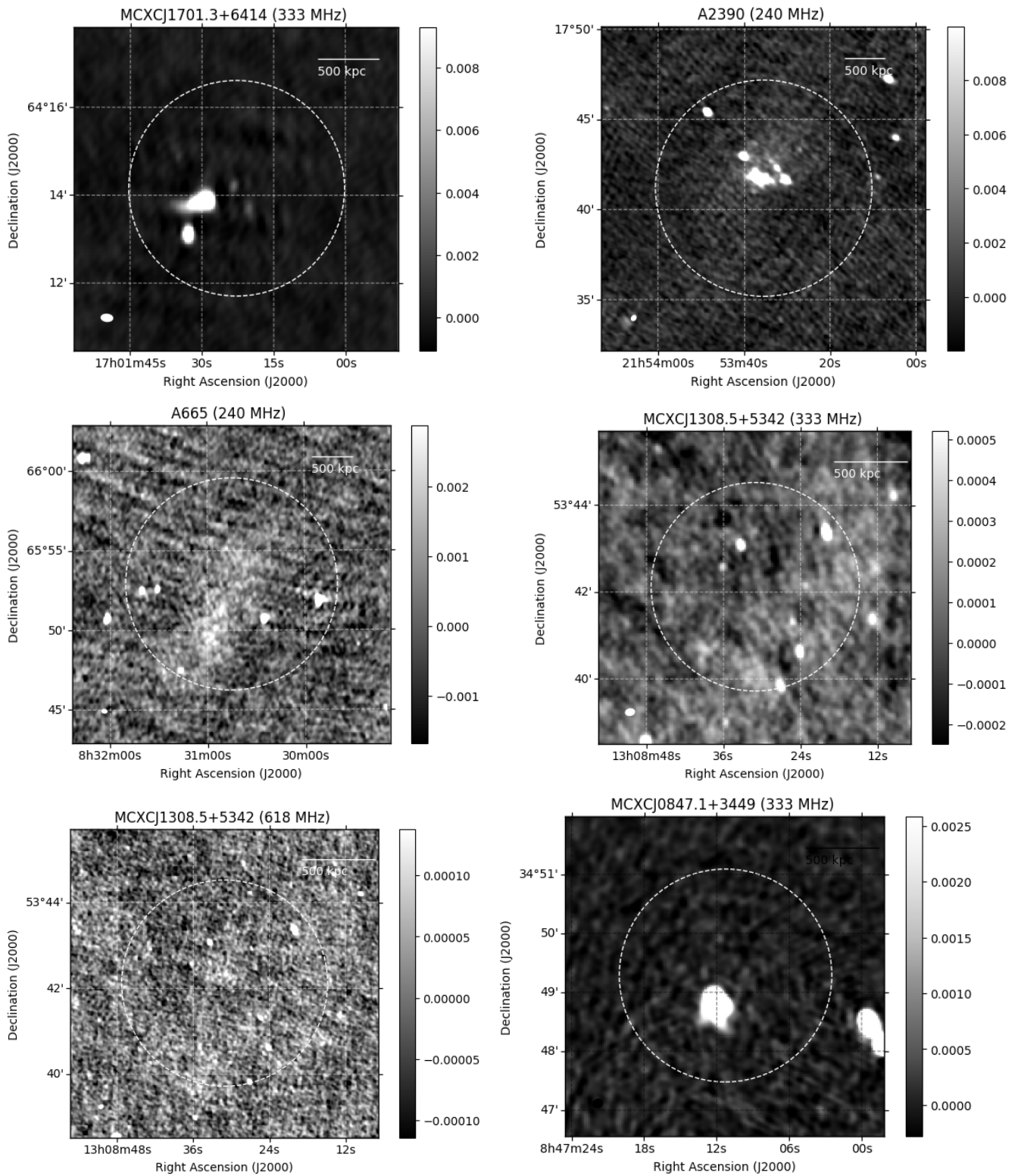


(b) Radio images contd.



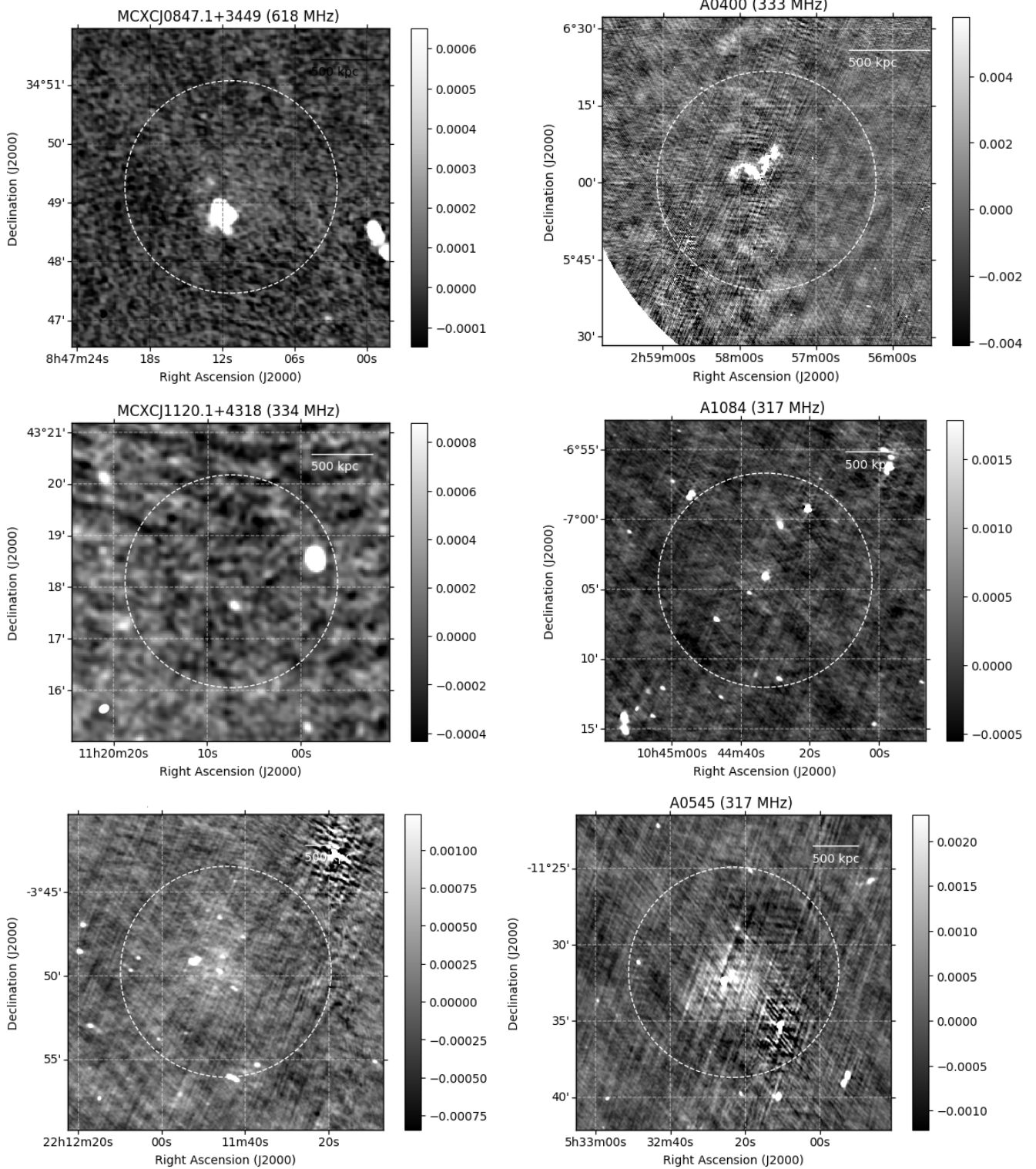
(c) Radio images contd.



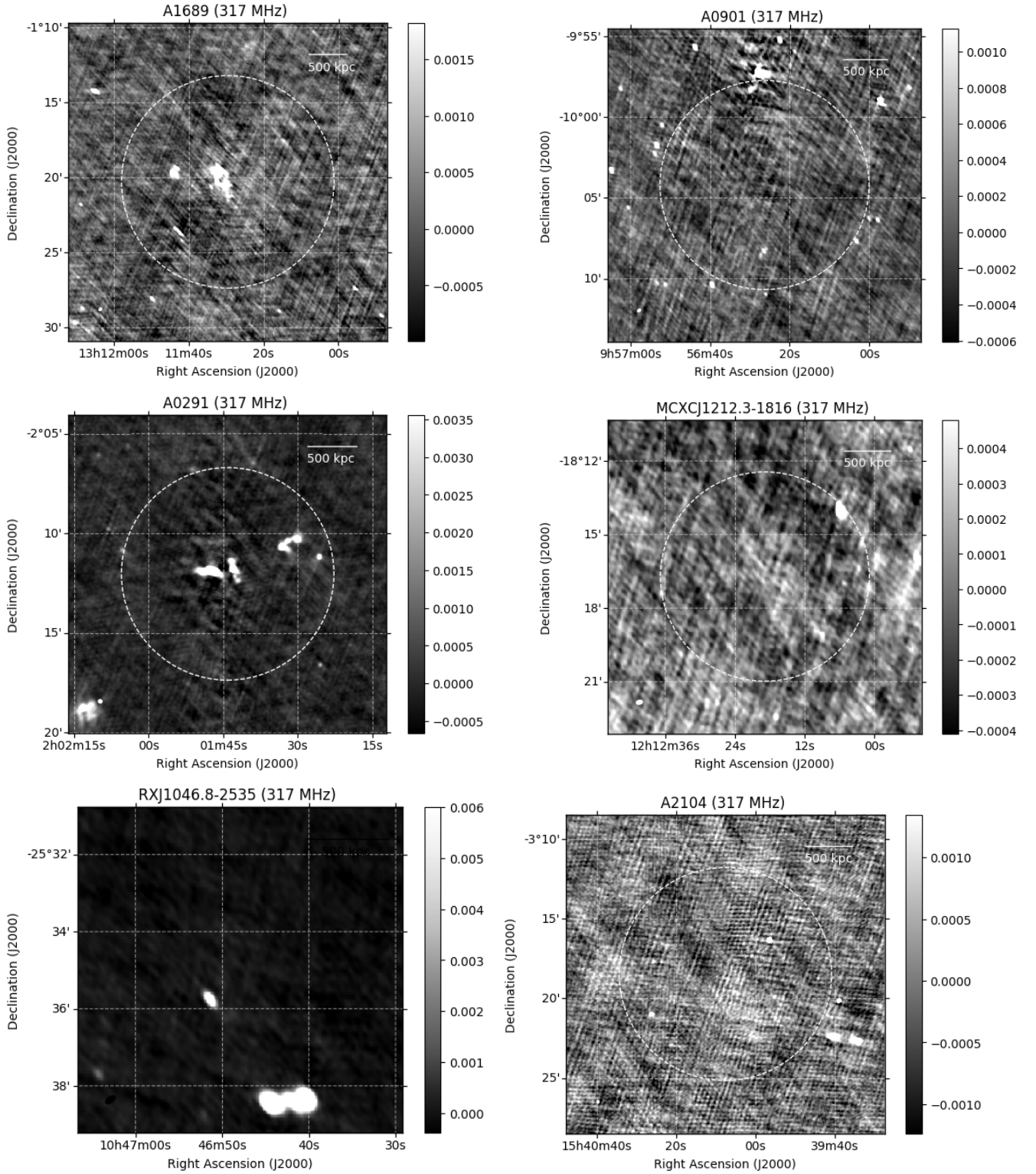


(d) Radio images contd.



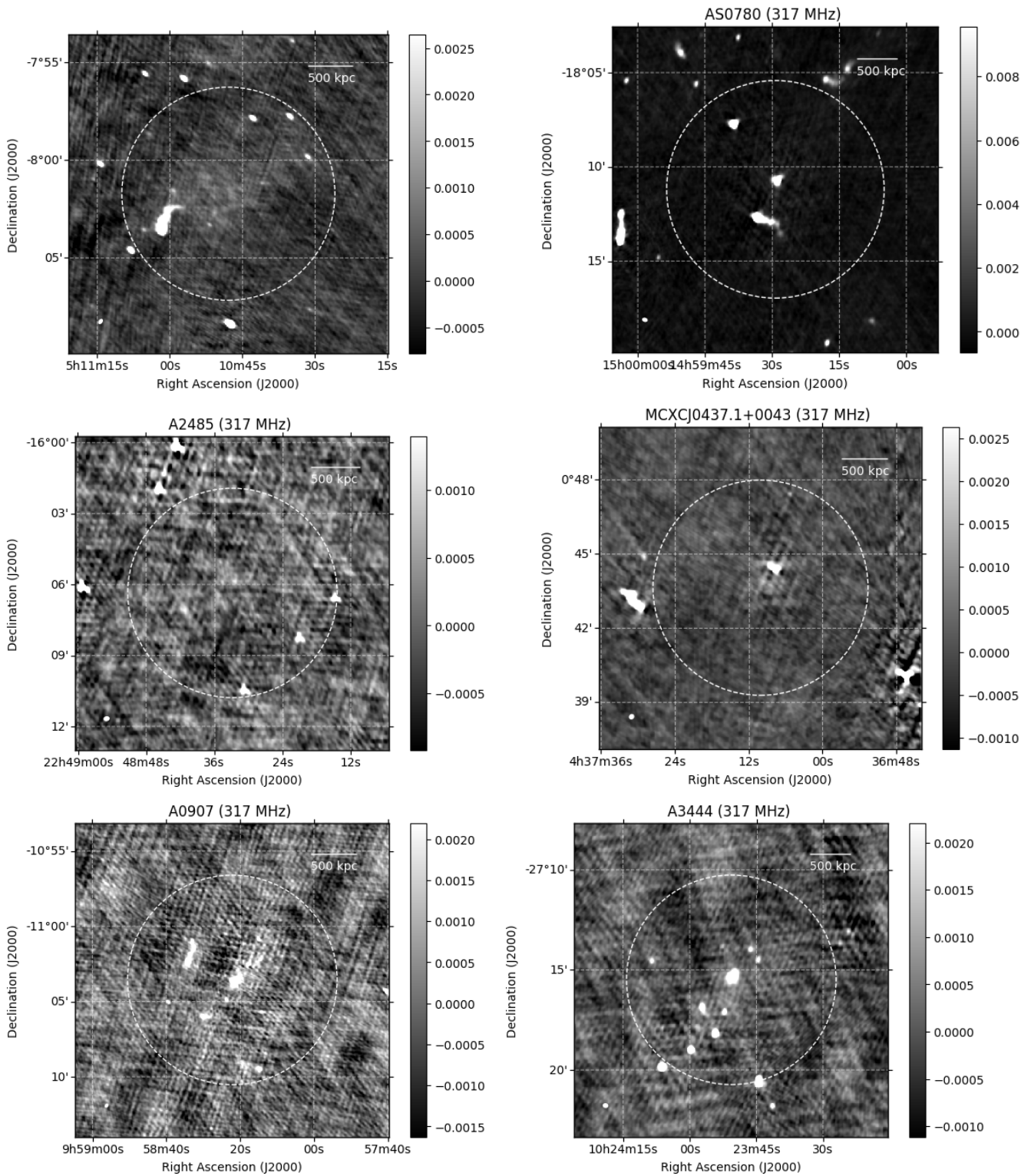


(e) Radio images contd.

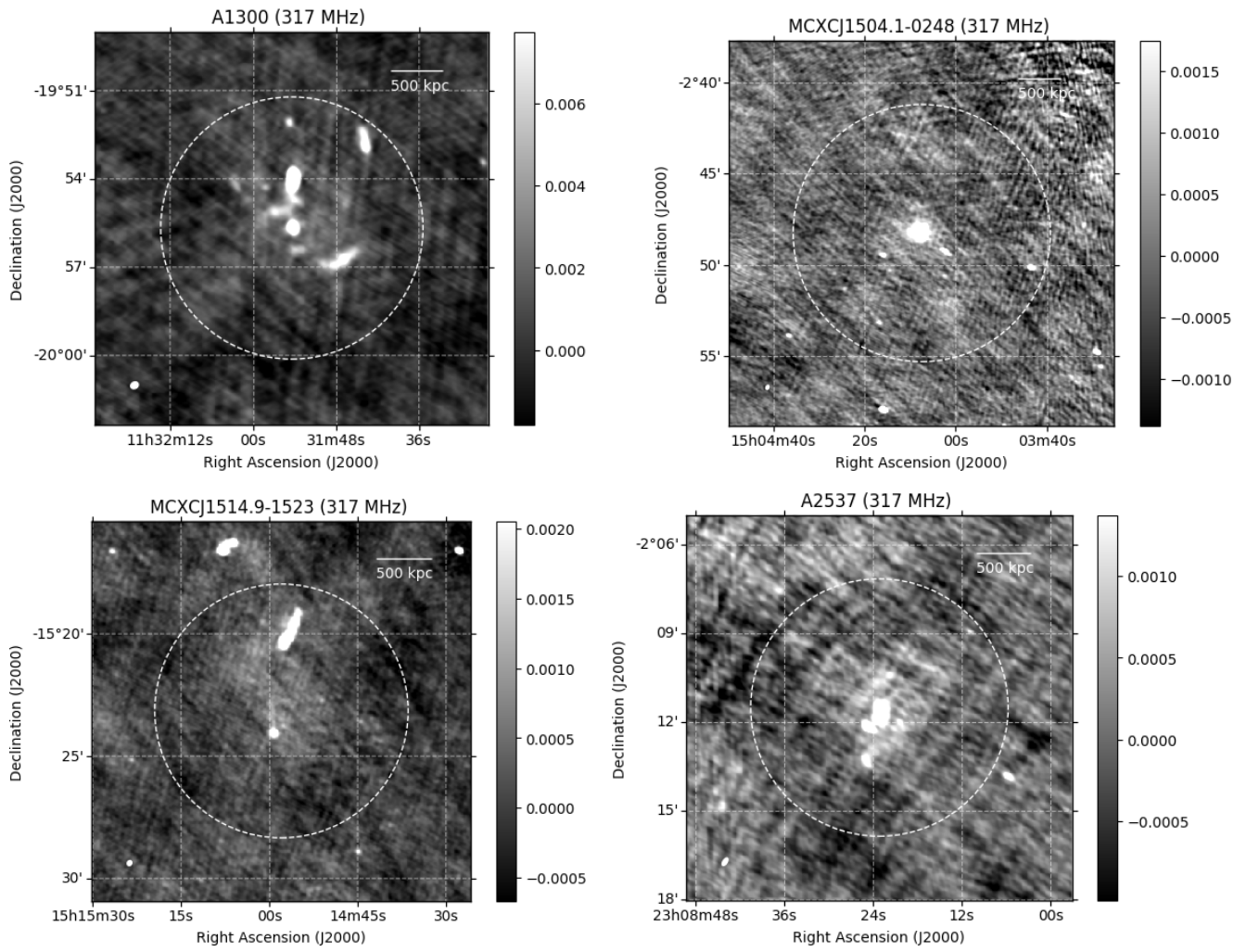


(f) Radio images contd. Note that no  $R_{500}$  circle is shown for RXJ1046.8-2535 since no X-ray information is available for that cluster.





(g) Radio images contd.



(h) Radio images contd.